Submitted to ApJ
Preprint typeset using LaTeX style emulateapj v. 08/22/09

CONSTRAINTS ON COSMOLOGY FROM THE COSMIC MICROWAVE BACKGROUND POWER SPECTRUM OF THE 2500 deg^2 SPT-SZ SURVEY

Z. Hou,[1] C. L. Reichardt,[2] K. T. Story,[3,4] B. Follin,[1] R. Keisler,[3,4] K. A. Aird,[5] B. A. Benson,[3,6] L. E. Bleem,[3,4] J. E. Carlstrom,[3,4,6,7,8] C. L. Chang,[3,6,8] H-M. Cho, [9] T. M. Crawford,[3,7] A. T. Crites,[3,7] T. de Haan,[10] R. de Putter,[12,13] M. A. Dobbs,[10] S. Dodelson,[3,7,11] J. Dudley,[10] E. M. George,[2] N. W. Halverson,[14] G. P. Holder,[10] W. L. Holzapfel,[2] S. Hoover,[3,4] J. D. Hrubes,[5] M. Joy,[15] L. Knox,[1] A. T. Lee,[2,16] E. M. Leitch,[3,7] M. Lueker,[13] D. Luong-Van,[5] J. J. McMahon,[17] J. Mehl,[8,3] S. S. Meyer,[3,4,6,7] M. Millea,[1] J. J. Mohr,[18,19,20] T. E. Montroy,[21] S. Padin,[3,7,13] T. Plagge,[3,7] C. Pryke,[3,6,7,22] J. E. Ruhl,[21] J.T. Sayre,[21] K. K. Schaffer,[3,6,23] L. Shaw,[10] E. Shirokoff,[2] H. G. Spieler,[16] Z. Staniszewski,[21] A. A. Stark,[24] A. van Engelen,[10] K. Vanderlinde,[10] J. D. Vieira,[13] R. Williamson,[3,7] and O. Zahn[25]

Submitted to ApJ

ABSTRACT

We explore extensions to the ΛCDM cosmology using measurements of the cosmic microwave background (CMB) from the recent SPT-SZ survey, along with data from *WMAP*7 and measurements of H_0 and BAO. We check for consistency within ΛCDM between these datasets, and find some tension. The CMB alone gives weak support to physics beyond ΛCDM, due to a slight trend relative to ΛCDM of decreasing power towards smaller angular scales. While it may be due to statistical fluctuation, this trend could also be explained by several extensions. We consider running of the primordial spectral index ($dn_s/d\ln k$), as well as two extensions that modify the damping tail power (the primordial helium abundance Y_p and the effective number of neutrino species $N_{\rm eff}$) and one that modifies the large-scale power due to the integrated Sachs-Wolfe effect (the sum of neutrino masses $\sum m_\nu$). These extensions have similar observational consequences and are partially degenerate when considered simultaneously. Of the 6 one-parameter extensions considered, we find CMB to have the largest preference for $dn_s/d\ln k$ with $-0.046 < dn_s/d\ln k < -0.003$ at 95% confidence, which strengthens to a $2.7\,\sigma$ indication of $dn_s/d\ln k < 0$ from CMB+BAO+H_0. Detectable $dn_s/d\ln k \neq 0$ is difficult to explain in the context of single-field, slow-roll inflation models. We find $N_{\rm eff} = 3.62 \pm 0.48$ for the CMB, which tightens to $N_{\rm eff} = 3.71 \pm 0.35$ from CMB+BAO+H_0. Larger values of $N_{\rm eff}$ relieve the mild tension between CMB, BAO and H_0. When the Sunyaev-Zeldovich selected galaxy cluster abundances ($\rm SPT_{CL}$) data are also included, we obtain $N_{\rm eff} = 3.29 \pm 0.31$. Allowing for $\sum m_\nu$gives a $3.0\,\sigma$ detection of $\sum m_\nu > 0$ from CMB+BAO+H_0+$\rm SPT_{CL}$. The median value is (0.32 ± 0.11) eV, a factor of six above the lower bound set by neutrino oscillation observations. All datasets except H_0 show some preference for massive neutrinos; data combinations including H_0 favor nonzero masses only if BAO data are also included. We also constrain the two-parameter extensions $N_{\rm eff} + \sum m_\nu$ and $N_{\rm eff} + Y_p$ to explore constraints on additional light species and big bang nucleosynthesis respectively.

Subject headings: cosmic background radiation, cosmological parameters, early universe, inflation

[1] Department of Physics, University of California, One Shields Avenue, Davis, CA, USA 95616
[2] Department of Physics, University of California, Berkeley, CA, USA 94720
[3] Kavli Institute for Cosmological Physics, University of Chicago, 5640 South Ellis Avenue, Chicago, IL, USA 60637
[4] Department of Physics, University of Chicago, 5640 South Ellis Avenue, Chicago, IL, USA 60637
[5] University of Chicago, 5640 South Ellis Avenue, Chicago, IL, USA 60637
[6] Enrico Fermi Institute, University of Chicago, 5640 South Ellis Avenue, Chicago, IL, USA 60637
[7] Department of Astronomy and Astrophysics, University of Chicago, 5640 South Ellis Avenue, Chicago, IL, USA 60637
[8] Argonne National Laboratory, 9700 S. Cass Avenue, Argonne, IL, USA 60439
[9] NIST Quantum Devices Group, 325 Broadway Mailcode 817.03, Boulder, CO, USA 80305
[10] Department of Physics, McGill University, 3600 Rue University, Montreal, Quebec H3A 2T8, Canada
[11] Center for Particle Astrophysics, Fermi National Accelerator Laboratory, Batavia, IL, USA 60510
[12] Jet Propulsion Laboratory, California Institute of Technology, 4800 Oak Grove Drive, Pasadena, CA, USA 91109
[13] California Institute of Technology, MS 249-17, 1216 E. California Blvd., Pasadena, CA, USA 91125
[14] Department of Astrophysical and Planetary Sciences and Department of Physics, University of Colorado, Boulder, CO, USA 80309
[15] Department of Space Science, VP62, NASA Marshall Space Flight Center,Huntsville, AL, USA 35812
[16] Physics Division, Lawrence Berkeley National Laboratory, Berkeley, CA, USA 94720
[17] Department of Physics, University of Michigan, 450 Church Street, Ann Arbor, MI, USA 48109
[18] Department of Physics, Ludwig-Maximilians-Universität, Scheinerstr. 1, 81679 München, Germany
[19] Excellence Cluster Universe, Boltzmannstr. 2, 85748 Garching, Germany
[20] Max-Planck-Institut für extraterrestrische Physik, Giessenbachstr. 85748 Garching, Germany
[21] Physics Department, Center for Education and Research in Cosmology and Astrophysics, Case Western Reserve University,Cleveland, OH, USA 44106
[22] Department of Physics, University of Minnesota, 116 Church Street S.E. Minneapolis, MN, USA 55455
[23] Liberal Arts Department, School of the Art Institute of Chicago, 112 S Michigan Ave, Chicago, IL, USA 60603
[24] Harvard-Smithsonian Center for Astrophysics, 60 Garden Street, Cambridge, MA, USA 02138
[25] Berkeley Center for Cosmological Physics, Department of Physics, University of California, and Lawrence Berkeley National

1. INTRODUCTION

Measurements of the damping tail of the cosmic microwave background (CMB) power spectrum provide new insights into the spectrum of the primordial density fluctuations, the contents of the pre-recombination plasma, and, through the effect of gravitational lensing, the low-redshift properties of the universe. In this paper, we study the constraints that can be placed on extensions to the standard ΛCDM cosmological model by recent South Pole Telescope (SPT) CMB power spectrum measurements presented in a companion paper (Story et al. 2013, hereafter S12) and complementary lower-redshift probes. For each extension, we discuss both the cosmological constraints and the physical origin of these constraints.

As shown by S12, the SPT bandpowers lead to constraints on the six standard ΛCDM parameters that are consistent with and comparable to those from *WMAP*7 (Larson et al. 2011; Komatsu et al. 2011). The agreement is especially remarkable given that the smaller angular scales probed by the SPT data are sensitive to new physical effects that are unimportant on the larger angular scales probed by *WMAP*. The combination of SPT and *WMAP*7 data can be used to exploit these additional effects in order to improve constraints on the ΛCDM model and possible extensions.

Measurements of the damping tail of the CMB power spectrum are sensitive to the low-redshift universe through the gravitational lensing of the CMB as well as the angular-diameter distance to the last scattering surface. The lensing sensitivity introduces a second constraint on the late-time expansion rate that breaks the geometric degeneracy (Bond et al. 1997; Zaldarriaga et al. 1997) that exists in large-scale CMB data. Measurements of CMB lensing, like that recently reported by S12, can be used to constrain the mean curvature of the observable universe.

More importantly, the SPT data expand the angular range over which the CMB temperature power spectrum is probed, leading to improved measurements of the damping scale due to photon diffusion (Silk 1968) and the positions of acoustic peaks. Past CMB experiments have found evidence for a trend of decreasing power at high multipoles, relative to the predictions of the ΛCDM model conditioned on CMB measurements at $l \lesssim 1000$ (Hamann et al. 2010b; Dunkley et al. 2011; Keisler et al. 2011), a trend that persists with the inclusion of the full-survey SPT bandpowers. This trend may be thought of as a scale-dependent tilt in the CMB power spectrum, and we explore five one-parameter extensions to ΛCDM that effectively allow for such a scale-dependent tilt. These extensions are: allowing massive neutrinos ($\sum m_\nu$), introducing "running" of the spectral index of the primordial power spectrum ($dn_s/d\ln k$), varying the effective number of neutrino species ($N_{\rm eff}$), allowing the helium abundance (Y_p) to depart from the predictions of big bang nucleosynthesis (BBN), and allowing non-zero early dark energy ($\Omega_{\rm e}$). A unifying theme in this paper will be a preference for model extensions that can accommodate a scale-dependent tilt that becomes increasingly red at higher multipoles.

The CMB damping tail measurements do not add sensitivity to the dark energy equation of state w, since dark energy becomes important at late times and this parameter has little effect on the lensing amplitude. Therefore, we do not present constraints on ΛCDM+w in this paper, although we sometimes include w when exploring the effect of parameter degeneracies on the constraints for other parameters.

We explore two 2-parameter extensions to the ΛCDM model which are physically and theoretically motivated: ΛCDM+$N_{\rm eff}$+Y_p and ΛCDM+$N_{\rm eff}$+$\sum m_\nu$. The first case is an interesting consistency test of BBN. Both Y_p and $N_{\rm eff}$ are primarily constrained by measurements of the damping scale, however both can be constrained simultaneously since varying $N_{\rm eff}$ has the secondary effect of inducing a phase shift in the acoustic oscillations. The second extension, ΛCDM+$N_{\rm eff}$+$\sum m_\nu$, is a test of the possible existence of sterile neutrinos, which have been postulated with masses in the eV range in order to explain some neutrino oscillation anomalies (e.g., Aguilar et al. 2001; Aguilar-Arevalo et al. 2010; Mention et al. 2011).

While all of these extensions can be constrained with CMB data alone, low-redshift measurements add constraining power and provide consistency checks to the CMB data. We incorporate measurements of the Hubble constant (H_0), the baryon acoustic oscillation (BAO) feature of the matter power spectrum, luminosity distances from supernovae (SNe), the matter power spectrum inferred from a redshift catalog of luminous red galaxies (LRGs), and the abundance of Sunyaev-Zel'dovich (SZ)-selected clusters. We pay particular attention to the BAO and H_0 measurements, specifically the Anderson et al. (2012) BAO measurement at $z = 0.57$ and the Riess et al. (2011) determination of H_0, because they are highly precise constraints that interact in an interesting way with those from the CMB. We quantify the level of consistency between the CMB, BAO, and H_0 datasets in the context of the ΛCDM model, and we study which model extensions are preferred by the CMB-only and combined CMB+BAO+H_0 datasets.

Throughout this work, we make a point of explaining the physical mechanisms behind the constraints we find. That is, we address questions such as, "How are the neutrino masses constrained?" and "What features in the data explain the preference for nonzero masses?" We also clarify what other extensions might explain the same features in the data.

The structure of the paper is as follows. We briefly describe the analysis methodology and data from the SPT and other experiments used in this analysis in § 2. The physical origins of the CMB constraints on the standard ΛCDM cosmology are presented in § 3. We discuss the consistency between datasets, and the evidence for extensions to the ΛCDM model in § 4. We study the physical origins of the constraint on non-zero curvature in § 5. We consider massive neutrinos in § 6 and running of the scalar index in § 7. Other single-parameter extensions – $N_{\rm eff}$, Y_p, and $\Omega_{\rm e}$ – are discussed in § 8. We consider 2-parameter extensions in § 9. Finally, we conclude in § 10.

2. PRELIMINARIES

Here we introduce the datasets that will be used in the cosmological parameter fitting. We also describe the

Laboratory, Berkeley, CA, USA 94720

Markov Chain Monte Carlo (MCMC) methods that will be used to fit cosmological parameters.

2.1. *CMB Power Spectrum Measurements*

In this work, we will use CMB bandpowers from *WMAP* and SPT, and will refer to the combined dataset as the "CMB" dataset. The *WMAP* data we use are the measurements of the CMB power spectrum at $2 \leq l \leq 1200$ from the *WMAP* 7-year release (Larson et al. 2011).[26] We will focus on the new SPT power spectrum results presented by S12, hereafter referred to as the SPT dataset. The SPT bandpowers represent a two-fold improvement over the best previous measurement (Keisler et al. 2011, K11) of the CMB power spectrum at $l > 800$. We briefly summarize the analysis of S12 and review the modeling of the contributions from extragalactic foregrounds.

The full SPT-SZ survey was completed in November 2011 and covers $\sim$2500 deg^2 in three frequency bands at 95, 150, and 220 GHz. The SPT bandpowers used in this work are based on the 150 GHz data from the complete survey. As in earlier SPT power spectrum analyses, the bandpowers are calculated using a pseudo-C_l method. The bandpowers cover the range $650 < l < 3000$ and are sample-variance limited at $l < 2900$. The covariance matrix contains terms for the sample and noise variances as well as beam and calibration uncertainties. Beams are estimated through a combination of observations of planets and bright synchrotron sources in the survey fields. The bandpowers are calibrated with an accuracy of 2.6% in power by comparing the SPT and *WMAP* 7-year power over the multipole range $l \in [650, 1000]$.

We model contributions from extragalactic foregrounds to the SPT bandpowers exactly as in S12. Using the notation $D_l \equiv l(l+1)C_l/(2\pi)$ these are given by

$$D_l^{\rm fg} = D_{3000}^{\rm PS}\left(\frac{l}{3000}\right)^2 + D_{3000}^{\rm CL}\left(\frac{l}{3000}\right)^{0.8} + D_{3000}^{\rm SZ} f_l^{\rm SZ} \quad (1)$$

where $D_{3000}^{\rm PS}$, $D_{3000}^{\rm CL}$, and $D_{3000}^{\rm SZ}$ are the amplitudes at $l = 3000$ for the Poisson point source power, clustered point source power, and total SZ power spectrum respectively, and $f_l^{\rm SZ}$ gives the l-dependence of the SZ power spectrum as modeled in Shaw et al. (2010). We apply Gaussian priors on these amplitudes of $D_{3000}^{\rm PS} = 19.3 \pm 3.5\,\mu{\rm K}^2$, $D_{3000}^{\rm CL} = 5.0 \pm 2.5\,\mu{\rm K}^2$, and $D_{3000}^{\rm SZ} = 5.5 \pm 3.0\,\mu{\rm K}^2$ (Shirokoff et al. 2011). We include the SZ term in the *WMAP*7 likelihood calculation, but we do not include the two point source terms since the *WMAP*7 likelihood code already marginalizes over appropriate point source terms. We have tested that all parameter constraints are insensitive to loosening the assumed extragalactic foreground priors.

As was argued by S12, we expect galactic foregrounds to have negligible impact on the SPT bandpowers and do not include a contribution from them in the bandpower modeling. The SPT and *WMAP*7 bandpowers are shown in the upper panel of Figure 1 plotted with the best-fit ΛCDM model, including the best-fit extragalactic foreground model consistent with the prior presented above. The residual between the data and this best-fit model is shown in the lower panel.

[26] A few days prior to submission, the WMAP collaboration released the 9-year data (Hinshaw et al. 2012; Bennett et al. 2012). Due to time constraints and the consistency of the 9-year data with the 7-year data, we chose not to incorporate the new data into this work.

2.2. *External Datasets*

Low-redshift observations can substantially inform the constraints on some cosmological parameters, particularly those parameters with impact at late times such as the mean curvature of the observable universe. We include these low-redshift datasets in many of the cosmological constraints presented in this work. These datasets are described below.

2.2.1. *Baryon Acoustic Oscillations*

BAO measurements use the spatial correlation of galaxies to constrain the comoving size of the sound horizon at the epoch when baryons and photons decouple, $r_s(z_{\rm drag})$. This redshift, $z_{\rm drag}$, is defined by $\tau_b(\eta(z_{\rm drag})) = 1$, where

$$\tau_b(\eta) \equiv \int_\eta^{\eta_0} a\sigma_T n_e d\eta'/(1 + \frac{3\rho_b}{4\rho_\gamma}) \,. \quad (2)$$

Here η is conformal time with η_0 the conformal time today, a is the scale factor, ρ_b and ρ_γ are the baryon and photon densities, n_e is the number density of free electrons, and σ_T is the Thomson cross section. The BAO feature in the galaxy correlation function can be observed as a function of both angular and redshift separations. Thus galaxy surveys can, in principle, constrain both $D_A(z)/r_s(z_{\rm drag})$ and $H(z)r_s(z_{\rm drag})$. However, the current generation of BAO observations typically reports constraints on a hybrid quantity, $r_s(z_{\rm drag})/D_V(z_{\rm eff})$ (henceforth r_s/D_V), where $D_V^3(z) = D_A^2(z)cz/H(z)$, c is the speed of light and $z_{\rm eff}$ is the effective redshift for the population of galaxies in the survey.

We use measurements of r_s/D_V from the following experiments: SDSS at $z_{\rm eff} = 0.35$ (Padmanabhan et al. 2012), BOSS at $z_{\rm eff} = 0.57$ (Anderson et al. 2012), and WiggleZ at $z_{\rm eff} = 0.44, 0.6$, and 0.73 (Blake et al. 2011). All of these experiments report r_s/D_V (or its inverse) using the fitting formula for $z_{\rm drag}$ presented by Eisenstein & Hu (1998). We numerically calculate $r_s(z_{\rm drag})$ with CAMB (Lewis et al. 2000). To account for the difference between $z_{\rm drag}$ as calculated by the fitting formula with $z_{\rm drag}$ as calculated by CAMB, Hamann et al. (2010a) find it necessary to rescale r_s by a factor 154.66/150.82. Mehta et al. (2012) show this constant rescaling adequately accounts for the differences in $z_{\rm drag}$ over the range of baryon density and matter density allowed by *WMAP*7. We therefore apply this rescaling to the reported r_s/D_V data for all parameter fitting.

2.2.2. *The Hubble Constant*

In contrast to the BAO approach to measuring cosmological distances, which starts from a known distance scale at $z \sim 1100$, measurements of the Hubble constant are based on the classic distance ladder which is built outwards from the solar system. Riess et al. (2011) use 253 Type 1a SNe to reach out into the Hubble flow and calibrate their luminosity distances with over 600 Cepheid variable stars in the host galaxies of eight nearby

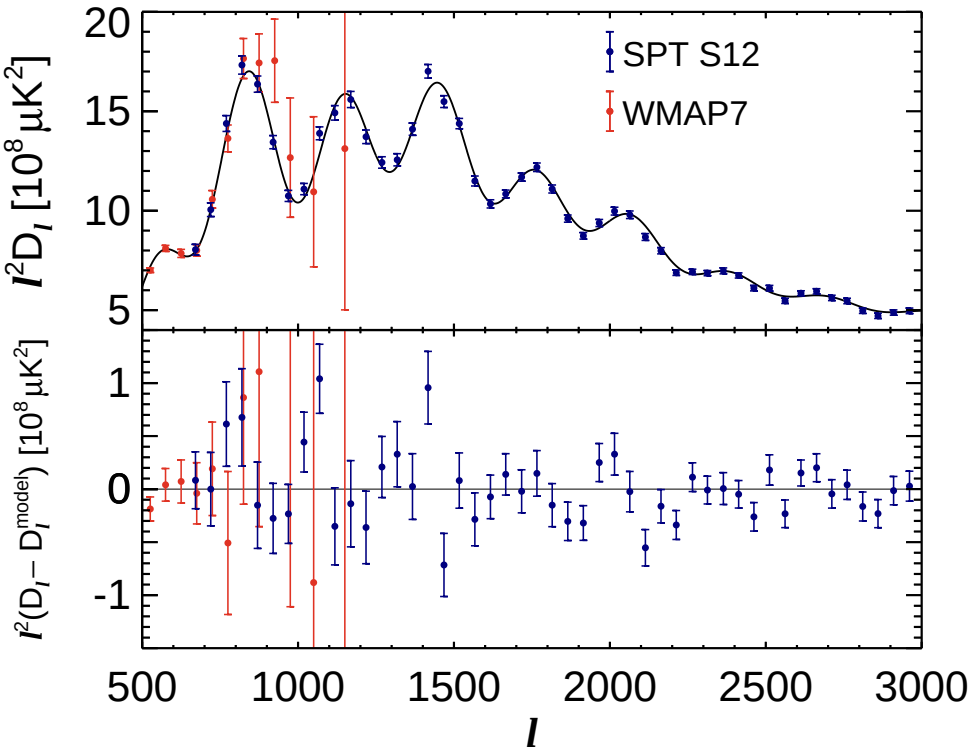

FIG. 1.— *Upper:* the SPT bandpowers from S12 (dark blue) and *WMAP*7 TT bandpowers (red) with $l \in [500, 3000]$. The solid curve shows the best-fit ΛCDM model including the best-fit extragalactic foreground components with priors for the combination of SPT and *WMAP*7 data. An additional normalization factor of l^2 has been applied to enhance the feature of the CMB damping tail. *Lower:* the residual between the data and the best-fit ΛCDM model with extragalactic foregrounds. As discussed in S12, the data are consistent with the standard cosmology.

Type 1a SNe. The Cepheids are calibrated in turn with three different methods, including 13 with trigonometric parallax. Accounting for both statistical and systematic sources of uncertainty, Riess et al. (2011) conclude that $H_0 = 73.8 \pm 2.4$ km/s/Mpc.

Freedman et al. (2012) recently released a new analysis of the HST Key Project, with a *Spitzer*-based calibration of the Cepheid distance scale, in which they find $H_0 = 74.3 \pm 2.1$ km/s/Mpc. As we had already completed many of the Markov chains used in this work, we chose not to rerun with this slightly improved constraint. We note that the tension in the ΛCDM model between BAO and H_0 discussed later would mildly increase with this new data since the measured H_0 value increases by $0.2\,\sigma$, and the uncertainty decreases by $\sim 10\%$.

2.2.3. *Luminosity Distances from Supernovae*

Type Ia SNe, employed as standardizable candles, remain the most precise means to extend the distance ladder to redshifts that are sensitive to cosmic acceleration. We use a sample of 427 SNeIa assembled by Conley et al. (2011) to constrain the luminosity distance. We follow the treatment in Sullivan et al. (2010) to handle the dependence of supernovae absolute magnitude on host galaxy stellar mass. We follow the approach of Conley et al. (2011) to marginalize over systematic uncertainties related to the uncertain intrinsic properties of supernovae.

2.2.4. *Matter Power Spectrum from SDSS DR7 LRG*

Reid et al. (2010) use a catalog of luminous red galaxies from the seventh data release of the Sloan Digital Sky Survey (SDSS DR7) to reconstruct the dark matter halo density field at $z \lesssim 0.4$ over nearly 8,000 deg^2. They use the reconstructed density field to determine the matter power spectrum over the range $0.02 < k < 0.2\,h\mathrm{Mpc}^{-1}$. We use their published likelihood code to incorporate this information in cosmological constraints. The information is primarily from the shape of the spectrum since the unknown halo masses, and therefore unknown biases, prevent the amplitude of the measured matter power spectrum from being used.

2.2.5. *SPT SZ-selected Clusters*

Reichardt et al. (2013, R12) present a catalog of 224 galaxy cluster candidates selected by their SZ significance from the first 720 deg^2 of sky surveyed by the SPT. As in R12, we use only the 100 cluster candidates at $z > 0.3$ with a significance greater than five. The optical properties of these systems are detailed by Song et al. (2012). X-ray Y_X measurements of 14 of the clusters are also used in the cosmological constraints; these measurements have been described by Andersson et al. (2011) and Benson et al. (2013). For brevity, we only include the cluster data in models showing a clear correlation between the model extension and the quantity $\sigma_8(\Omega_m/0.25)^{0.47}$. Vikhlinin et al. (2009) have shown that

this quantity is well constrained by cluster abundance data. Given a CMB+BAO+H_0 prior, we find such a correlation, and thus include the cluster data, for two extensions, $\sum m_\nu$ and $N_{\rm eff}$.

2.3. *Parameter Estimation Methodology*

Posterior probability distributions for the parameters are calculated using Markov Chain Monte Carlo (MCMC) methods (Christensen et al. 2001) with the publicly available CosmoMC[27] package (Lewis & Bridle 2002). We have modified the code to include the foreground terms from § 2.1 and the extensions to ΛCDM detailed in later sections; these modules and instructions for compiling them are available at the SPT website[28]. As can be inferred from Figure 1, the *WMAP*7 bandpowers are noise dominated on the multipoles measured by the SPT. The correlation between the two datasets is thus negligible, and we treat the two datasets as independent in this work.

We use the high_accuracy_default option in CosmoMC, and by default call the January 2012 version of CAMB (Lewis et al. 2000) to calculate the CMB and matter power spectra. Unless otherwise noted (for instance in § 6.2), we will report parameter constraints based on the median value of the posterior distribution with $1\,\sigma$ error bars defined based on the interval that includes the central 15.85% to 84.15% of the MCMC samples. For cases when we compare a parameter to some fiducial value (e.g. an extension parameter to its ΛCDM-consistent value), we report–unless otherwise noted–a significance in σ based on the Gaussian z-score of the probability above (or below) the fiducial value.

We will present parameter constraints on a spatially flat, gravitationally lensed ΛCDM model along with selected one- and two-parameter extensions to this model. The properties of the standard ΛCDM model are specified by six parameters: the optical depth to reionization (τ), the baryon density ($\Omega_b h^2$), the cold dark matter density ($\Omega_c h^2$), the angular scale of the sound horizon at last scattering (θ_s), the scalar spectral index (n_s), and the amplitude of primordial scalar perturbations at wavenumber $k = 0.05\,{\rm Mpc}^{-1}$ (Δ^2_R). Throughout this paper, we will use the notation $\omega_x \equiv \Omega_x h^2$. Since $\Omega_x \equiv \rho_x/\rho_c$, where $\rho_c = 3H_0^2/(8\pi {\rm G})$ is the critical density, ω_x is independent of the Hubble constant. We define the total matter density as the sum of baryons and cold dark matter, so that $\omega_m = \omega_b + \omega_c$. All densities are evaluated at the present epoch.

To speed up parameter estimation, we make use of the Boltzmann code emulator PICO (Fendt & Wandelt 2007b,a). PICO works by empirically modeling the CMB and matter power spectra as sums of polynomials, with the (cosmological parameter-dependent) polynomial coefficients determined by fitting them to output from CAMB. We have trained PICO for a 10-parameter model that includes the six ΛCDM parameters as well as $Y_{\rm P}$, $N_{\rm eff}$, $\sum m_\nu$, and $dn_s/d\ln k$. We use PICO instead of CAMB when working with any subset of this model space. Evaluating the power spectrum with PICO is several orders of magnitude faster than doing so with CAMB, and is even more accurate due to its training on CAMB runs with higher numerical accuracy than the high_accuracy_default setting. The PICO code and results of this training are available at the PICO website.[29]

[27] http://cosmologist.info/cosmomc - January 2012 version
[28] http://pole.uchicago.edu/public/data/story12/

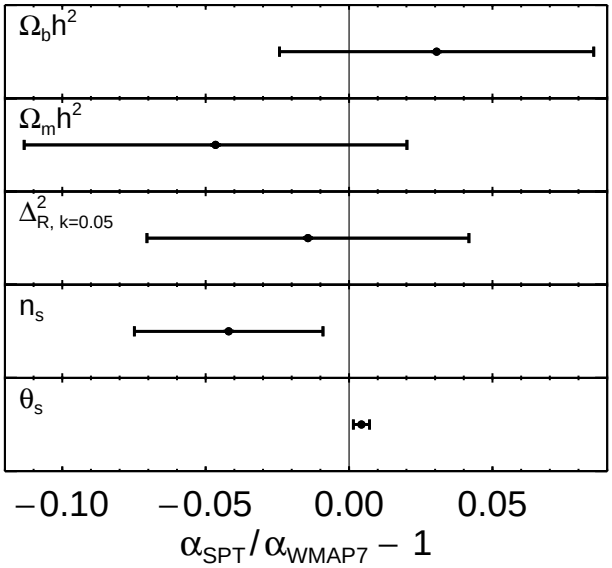

FIG. 2.— This figure illustrates the agreement between parameter values derived from the SPT and *WMAP*7 bandpowers. For each ΛCDM parameter, we plot the fractional change in the parameter, defined by $(\alpha_{\rm SPT}/\alpha_{WMAP7} - 1)$, and the error bar for this quantity. Following S12, the amplitude of scalar perturbations, Δ^2_R, is evaluated at $k = 0.05$ Mpc^{-1}. The optical depth to reionization is not plotted, as a *WMAP*7-based prior is used in the fits to the SPT bandpowers. The most significant shift is to the sound horizon scale which increases by $1.5\,\sigma$.

3. ΛCDM RESULTS

In this section, we consider the SPT-only and *WMAP*7-only constraints on the ΛCDM model parameters. As shown by S12 and Figure 2, the parameters estimated from the two datasets are consistent. Here we focus on the physical origins of the baryon and matter density constraints derived from different angular scales probed by *WMAP*7 and SPT. For each case, we begin by briefly reviewing the origins of the *WMAP*7 constraints (see, e.g., Hu & Dodelson 2002) and then discuss the origins of the SPT constraints. As we will see in later sections, understanding these mechanisms provides a foundation from which to explore other datasets and model extensions.

The *WMAP*7 constraint on the matter density ω_m derives from differences in the acoustic oscillations during the radiation-dominated and matter-dominated epochs. Modes that "enter the horizon"[30] during radiation domination receive a boost to their amplitude from the decay of the gravitational potential that occurs during their first compression into potential wells. In an expanding universe, the plasma would need to collapse at the free-fall (pressureless) rate to preserve the potential. The pressure support of the plasma slows the collapse, leading to a decaying gravitational potential. The decay boosts

[29] `https://sites.google.com/a/ucdavis.edu/pico`
[30] The horizon expands with time; a Fourier mode enters the horizon when its wavelength equals the horizon size.

the oscillation amplitude since modes gain more energy during the compression into the initially larger potential well than they later lose during the expansion out of the much reduced potential well. Modes entering during matter domination do not see such a boost, since the potential is predominantly sourced by pressureless dark matter. The difference in the oscillation amplitudes allows us to determine the angular scale separating modes that entered the horizon during matter domination from those that entered during radiation domination, $\theta_{\rm eq}$, which can be related to the redshift of matter-radiation equality, $z_{\rm eq}$. Because the radiation density, $\omega_{\rm rad}$, is completely specified in the ΛCDM model by the well-known temperature of the microwave background today and assumptions about neutrino production, this measurement of $z_{\rm eq}$ corresponds to a determination of ω_m through the relation $1 + z_{\rm eq} = \omega_m/\omega_{\rm rad}$.

The angular scales probed by the SPT bandpowers correspond to modes that entered the horizon in the radiation-dominated era, since the transition occurs around $l_{\rm eq} = \pi/\theta_{\rm eq} \simeq 434$. Thus the SPT bandpowers are largely insensitive to ω_m through the mechanism described above. To confirm this, we have tested removing the largest scales (third peak, $l < 1000$) from the SPT bandpowers and find only a minimal (5%) degradation of the SPT-only ω_m constraint. The SPT data are instead sensitive to the amplitude of gravitational lensing which in turn depends on ω_m. Gravitational lensing of the CMB smooths out the peak-trough structure of the CMB power spectrum, allowing lensing to be detected in the SPT power spectrum. The magnitude of the lensing potential power spectrum increases with ω_m. To support the claim that the SPT bandpowers determine ω_m through its effect on the amplitude of the lensing power spectrum, we have tested removing the lensing amplitude information. We accomplish this by rescaling the lensing power spectrum, $C_l^{\phi\phi}$, by a free parameter, A_L, defined by:

$$C_l^{\phi\phi} \rightarrow A_L C_l^{\phi\phi}. \quad (3)$$

Marginalizing over A_L doubles the uncertainty on ω_m, degrading the constraint from $\omega_m = 0.1286 \pm 0.0071$ to $\omega_m = 0.129 \pm 0.013$. When SPT and *WMAP*7 data are combined, ω_m is primarily constrained through its impact on $\theta_{\rm eq}$.

The *WMAP*7 constraint on ω_b derives from the relative heights of the even and odd acoustic peaks. The baryon density affects the plasma's pressure, which impacts the acoustic oscillations. Changing the pressure has opposite effects on compression into gravitational potential wells (odd peaks) versus compression onto gravitational potential hills (even peaks). The net result is that increasing ω_b raises the odd peaks relative to the even peaks.

The SPT constraint on baryon density is primarily derived from the same even/odd peak modulation. Due to the decay of the gravitational potentials, the even/odd modulation of peak heights is suppressed on smaller scales. The dominant constraining power in the SPT data is from the height of the third acoustic peak. Increasing ω_b at fixed $z_{\rm eq}$ and θ_s increases the height of the third acoustic peak relative to higher peaks. If we remove the SPT bandpowers over the third acoustic peak (dropping all bandpowers at $l < 1000$), the SPT-only constraint on ω_b degrades by nearly a factor of 2 from $\omega_b = 0.0230 \pm 0.0011$ to $\omega_b = 0.0236 \pm 0.0020$.

The damping scale provides a second (weaker) lever arm to constrain the baryon density from the SPT data. Photons are imperfectly coupled to baryons in the primordial plasma, and the resulting photon diffusion damps the acoustic oscillations. This photon diffusion is described by the diffusion length r_d, the root mean squared comoving distance a photon has traveled over the time in which the scale factor grows from 0 to a_* (the scale factor at decoupling). The diffusion length is given approximately by

$$r_d^2 = \pi^2 \int_0^{a_*} \frac{da}{a^3 \sigma_T n_e H} \left[\frac{R^2 + \frac{16}{15}(1+R)}{6(1+R^2)} \right]. \quad (4)$$

Here n_e is the number density of free electrons, σ_T is the Thompson cross-section, and $R = 3\rho_b/(4\rho_\gamma)$. The factor in square brackets is due to the directional and polarization dependence of Thompson scattering (Kaiser 1983; Zaldarriaga & Harari 1995). The diffusion length is affected by ω_b through the number density of free electrons, $n_e(z) \propto X_e(z)\omega_b\,(1 - Y_p)$, where $X_e(z)$ is the fraction of Hydrogen atoms that are ionized and Y_p is the primordial fraction of baryonic mass in helium.

We quantify the importance of the SPT damping scale measurement in constraining the baryon density by introducing Y_p as a free parameter. At fixed ω_b, varying Y_p only impacts the free electron density and hence the diffusion scale. When we allow Y_p to vary freely, the uncertainty on ω_b slightly increases from 0.0011 to 0.0013. Thus, the primary sensitivity of the SPT data to the baryon density is from the measurement of the third acoustic peak rather than damping scale.

The SPT constraints on the other ΛCDM model parameters are based on similar physical mechanisms to the *WMAP*7 constraints. The angular size of the sound horizon, θ_s is constrained via the peak locations, while the primordial parameters n_s and $\Delta^2_{\rm R}$ are constrained through their impact on the amplitude and tilt of the CMB power spectrum. As mentioned in S12, the SPT bandpowers do not constrain τ; we instead apply a prior based on the *WMAP*7 polarization measurements.

We note that there is a trend in the CMB data for decreasing power at higher multipoles, relative to fits to the ΛCDM model using data from $l \lesssim 1000$. In the ΛCDM model space, this deficit manifests as the downward shift in n_s between *WMAP*7 and SPT seen in Figure 2. As we shall see in later sections, model extensions that can accommodate this trend are somewhat preferred by the CMB data.

4. CONSISTENCY OF CMB, BAO, AND H_0 MEASUREMENTS AND EVIDENCE FOR EXTENSIONS TO THE STANDARD COSMOLOGICAL MODEL

Combining the BAO and H_0 measurements with the CMB will have important implications for the model extensions we consider. Here we investigate the consistency of these datasets with one another. Tension between two sets of data in the context of a ΛCDM model can be caused by (1) statistical fluctuations in the measured values, (2) an inaccurate or incomplete accounting of the uncertainties (or biases) in one or more of the datasets, or (3) the inadequacy of the cosmological model. We discuss the consistency between datasets in § 4.1 and discuss any evidence for extensions to the ΛCDM model in § 4.2.

TABLE 1
Relative Consistency Between Datasets in the ΛCDM Model

Dataset Comparison	Add. dof	$\Delta\chi^2$	corrected PTE
(CMB) *vs* ($+H_0$)	1	0.23	–
(CMB) *vs* ($+\mathrm{BAO_{SDSS}}$)	1	1.8	–
(CMB) *vs* ($+\mathrm{BAO_{WiggleZ}}$)	3	1.7	–
(CMB) *vs* ($+\mathrm{BAO_{BOSS}}$)	1	5.1	0.090
(CMB+H_0) *vs* (+BAO)	3	7.4	–
(CMB+BAO) *vs* ($+H_0$)	1	3.5	0.12

Top 4 rows: the relative consistency between the CMB and the individual low-redshift measurements. For each model, we calculate the $\Delta\chi^2$ between the $\chi^2_{\rm min}$ for the CMB dataset and the $\chi^2_{\rm min}$ for the CMB+(each low-redshift experiment). The least consistent, $\mathrm{BAO_{BOSS}}$, is shown in row four, along with the probability to get a larger $\Delta\chi^2$ given four dataset combinations, specifically: (corrected PTE) = $1-(1-PTE)^4$.

Bottom 2 rows: the $\Delta\chi^2$ between the CMB+H_0 and CMB+BAO+H_0 datasets combinations, and the CMB+BAO and CMB+BAO+H_0 combinations. For the least consistent comparison, (CMB+BAO) *vs* ($+H_0$), we show the probability to get a larger $\Delta\chi^2$ given two chances.

4.1. *Consistency between datasets*

In the context of the ΛCDM model, we quantify the consistency between two datasets, x and y, with the use of a symmetric $\Delta\chi^2$ statistic. We calculate $\Delta\chi^2 = \chi^2_{x+y} - \chi^2_x - \chi^2_y$ where χ^2_{x+y} is the minimum value of the χ^2 obtained for the joint $(x+y)$ dataset in the model M with a similar definition for χ^2_x and χ^2_y. We use a modified simulated annealing minimizer (Goffe et al. 1994) to find the minimum χ^2 point. The $\Delta\chi^2$ is proportional to a likelihood ratio statistic, and is also connected to a Bayesian evidence ratio in the case of normal probability distributions, as shown by Marshall et al. (2006). The expected distribution of $\Delta\chi^2$ is a χ^2 distribution with degrees of freedom (dof) $N_{\Delta\chi^2} = N_{x+y} - N_x - N_y$. Here N_x is the dof for dataset x. We then compare the observed value of $\Delta\chi^2$ with its expected distribution and find the probability to exceed (PTE) this observed value.

For example, to compare the consistency of the CMB dataset with the H_0 "dataset," we calculate $\chi^2_{\rm min,[CMB+H_0]} - \chi^2_{\rm min,[CMB]} - \chi^2_{\rm min,[H_0]}$=0.23. Because H_0 has only one datapoint while the model has six free parameters, we have $N_{H_0} = 0$, $N_{CMB} = X$, and $N_{CMB+H_0} = X+1$. Thus $\Delta\chi^2$ in this comparison should be drawn from a χ^2 distribution with 1 dof, and we find a PTE of 0.63.

As we are considering the consistency between the CMB and multiple datasets, we have a set of size N of these PTEs, where N corresponds to the number of dataset comparisons in the test. The minimum PTE should yield the strongest evidence of possible tension. We therefore compare the observed minimum PTE to the expected distribution of the minimum of a set of N uniformly distributed random variables to derive a "corrected PTE". Specifically, the corrected PTE α is derived from the uncorrected PTE α_0 by $\alpha = 1-(1-\alpha_0)^N$. The corrected PTE for $\Delta\chi^2$ represents a measure of tension between datasets under the assumption that the given model is correct, and the difference between datasets is due to random scatter in the measurements. A high PTE indicates the data are remarkably consistent, and low PTE indicates the presence of tension between the measurements. We note however that if the model is poor, the corrected PTE may not be a good representation of tension with the model.

In the top four rows of Table 1, we report the $\Delta\chi^2$ between the CMB and each individual low-redshift dataset in the ΛCDM model. Among the BAO datasets, the $\mathrm{BAO_{WiggleZ}}$ dataset has a low $\Delta\chi^2$ of 1.7 (3 dof), while the $\mathrm{BAO_{BOSS}}$ dataset has an unusually high $\Delta\chi^2$ of 5.1 (1 dof), driven in part by the high precision of this data point. The probability of getting a $\Delta\chi^2$ this large given 1 dof (un-corrected PTE) is 2.3%; in the case of 4 random draws (corresponding to the 3 BAO plus 1 H_0 datasets) from this $\Delta\chi^2$ distribution the probability of at least one being this high (corrected PTE) is 9.0%.

When the three BAO measurements are combined into a single dataset, the $\Delta\chi^2$ contributions from $\mathrm{BAO_{WiggleZ}}$ and $\mathrm{BAO_{BOSS}}$ balance out to give a more reasonable total $\Delta\chi^2$. Thus the CMB+BAO versus H_0 case has a lower PTE than the CMB+H_0 versus BAO case. The $\Delta\chi^2$ between CMB+BAO and H_0 is 3.5 for 1 dof, and the corresponding probability of getting a lower PTE given two random draws is 12%.

From Table 1, we see some degree of tension between the CMB and the BOSS BAO data point, and between CMB + BAO and H_0. Both of these tensions exist (to a lesser degree) with the *WMAP*7 data alone and have been noted by others (Anderson et al. 2012; Mehta et al. 2012). Anderson et al. (2012) highlighted the importance of ω_m for consistency between *WMAP*7 and BAO measurements, noting that a $1\,\sigma$ increase in ω_m from its *WMAP*7-inferred value would bring them into near-perfect agreement. Instead, the SPT+*WMAP*7 data prefer a slight downward shift in ω_m which, together with the decreased uncertainty, leads to the increased level of tension between BAO and the CMB in the ΛCDM model. At the same time, the shift in ω_m improves agreement of the CMB data with the H_0 measurement.

The relationship between ω_m and the CMB, BAO, and H_0 measurements can be seen in Figure 3. This figure shows the parameter space H_0 vs. $r_s/D_V(z=0.57)$ (the characteristic BAO parameter at the redshift reported by BOSS), which is the plane in parameter space that is constrained by the H_0 and $\mathrm{BAO_{BOSS}}$ datasets. When combined with any of the three combinations of SPT and *WMAP*7 data shown in this figure, the H_0 data prefers lower values of ω_m, while the BAO data prefers higher ω_m.

We find the apparent tension significant enough in some model spaces, including ΛCDM, to suggest caution in interpretation of the results. However, in no model spaces is the significance sufficient to rule out statistical fluctuations, and we have no evidence for either systematic biases or underestimated uncertainties in the data.

4.2. *Evidence for Extensions*

Two natural questions are: (1) which extensions to the ΛCDM model are preferred by the data, and (2) do these extensions ease or increase the tension between the

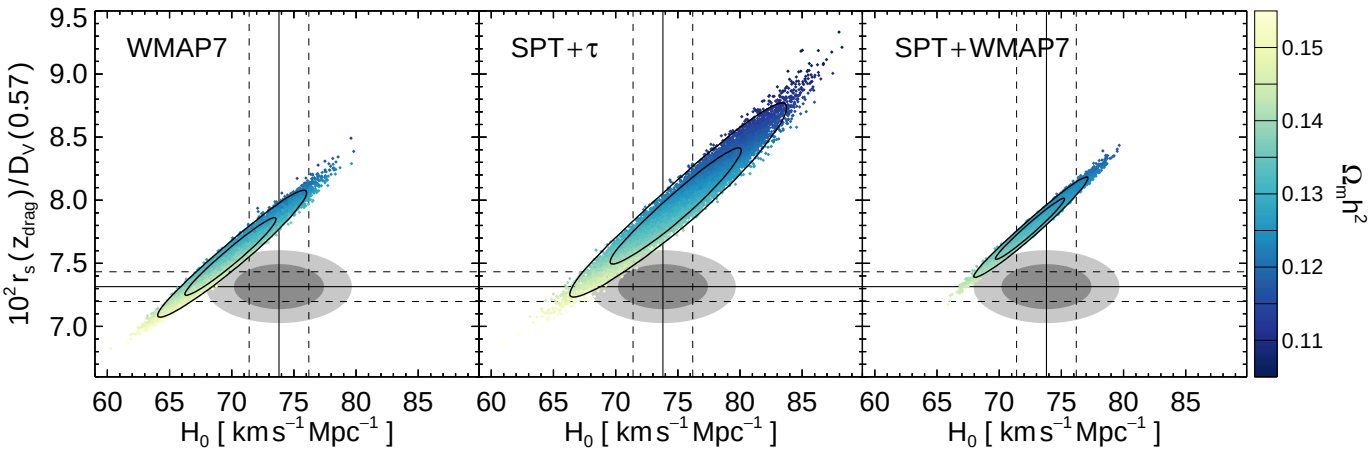

FIG. 3.— Here we illustrate the degree of consistency between the CMB data and the two external datasets which are in the most tension: BOSS and H_0. The solid lines mark the 1 and $2\,\sigma$ contours from the CMB data in the $H_0 - r_s/D_V(0.57)$ plane, while the color encodes the value of $\Omega_m h^2$, as shown in the color scale on the right. From left to right, the CMB data used is *WMAP*7, SPT+τ, and SPT+*WMAP*7. The horizontal solid and dashed lines mark the central value and $1\,\sigma$ region for the BOSS BAO measurement, while the vertical lines do the same for H_0. The joint 1 and $2\,\sigma$ likelihood regions for BOSS+H_0 measurements are denoted by the dark and light grey shaded contours.

datasets? Here we answer these two questions, then give physical explanations for the results.

We define a slightly different $\Delta\chi^2$ statistic to quantify how strongly the data prefer a given extension ϕ over the ΛCDM model: $\Delta\chi^2 = \chi^2_{\Lambda\rm CDM} - \chi^2_{\Lambda{\rm CDM}+\phi}$. A large reduction in $\chi^2_{\rm min}$ (equivalently a large $\Delta\chi^2$) relative to the baseline ΛCDM model indicates that the extended model is a much better fit to the data. For instance, if $\Delta\chi^2 = 4$ (6.2) for a given extension with one (two) degrees of freedom, this means that the data favor this extension at $2\,\sigma$. We consider models which are favored by more than $2\,\sigma$ to be "preferred" by the data. However, it is worth noting that we do not consider all possible physically motivated extensions, and also that a single feature in the data may lead to an apparent preference for multiple extensions with degenerate effects. The results of this statistic for the extensions we consider in this work are presented in Table 2.

The CMB dataset shows a $>2\,\sigma$ preference for the extensions ΛCDM+$dn_s/d\ln k$ and ΛCDM+Y_p. The $\Delta\chi^2$ for ΛCDM+$dn_s/d\ln k$ and ΛCDM+Y_p is 4.9 and 4.4 respectively. Allowing running or varying the helium abundance allows for an increasingly red, scale-dependent tilt, and provides a better match to the observed CMB bandpowers than does the ΛCDM model. All other single-parameter extensions are not significantly favored by the CMB data. The combined CMB+BAO+H_0 data show even stronger preference for these same model extensions, with $\Delta\chi^2$ for ΛCDM+$dn_s/d\ln k$ and ΛCDM+Y_p of 7.4 and 5.3, respectively.

The CMB alone prefers neither two-parameter extension at $>2\,\sigma$. Although the $\Delta\chi^2 = 5.5$ for the ΛCDM+$N_{\rm eff}$+Y_p model is higher than that of any single parameter extension given the CMB data, this is for two, instead of one, additional dof. The ΛCDM+$N_{\rm eff}$+$\sum m_\nu$ model is preferred by the CMB+BAO+H_0 combination, with $\Delta\chi^2 = 7.9$. As we will discuss later in this paper in § 9.2 and Figure 18, this model space also improves the consistency between the CMB, BAO, and H_0 datasets.

The ΛCDM+w model is not significantly preferred by either the CMB or the CMB+BAO+H_0 combination. Additionally, we find that adding the SPT bandpowers do not significantly improve w constraints. Therefore, we do not present constraints on ΛCDM+w in this paper, although we sometimes include w when exploring the effect of parameter degeneracies on the constraints for other parameters.

Next we explore the second question: how do these extensions affect the aforementioned tension between the CMB and low-redshift (BAO and H_0) measurements? This question is most clearly explored in the context of Figure 4. All the panels of this figure have the same x- and y-axes as Figure 3. The BAO$_{\rm BOSS}$ dataset has been singled out for two reasons. First, it is the most precise low-redshift BAO measurement; second, it has the most tension with the CMB and H_0 data in the ΛCDM model. Each panel of the figure shows color-coded samples from a CMB-only MCMC for a different cosmological model. The color coding reflects values of the extension parameter, thus showing how the chosen parameter moves within the CMB constraints in this parameter space.

Among the 1-parameter extensions, ΛCDM+$N_{\rm eff}$ is most effective at reconciling the CMB, BAO, and H_0 datasets. A thorough discussion of the physical and observational effects of $N_{\rm eff}$ is reserved for § 8.1, however, we briefly preview the important aspects here. The expansion of the CMB likelihood volume towards the BAO$_{\rm BOSS}$+H_0 constraint arises because increasing $N_{\rm eff}$ increases the expansion rate at early times which reduces the sound horizon length r_s. To match the measured CMB acoustic peak locations, one must also decrease D_A by increasing H_0. The net result, as discussed in Hou et al. (2013), is an increase in H_0 with minimal change to r_s/D_V. Thus, the contours for the ΛCDM+$N_{\rm eff}$ case resemble those for ΛCDM except expanded horizontally in H_0.

The extensions which become important primarily at late-times (Ω_k, w, and $\sum m_\nu$) have a smaller effect on r_s and instead influence the late-time geometry and thus the inverse distance measures $1/D_V$ and H_0. As a result, these extensions stretch the CMB contours along lines with positive slope in the H_0-r_s/D_V plane, as seen in

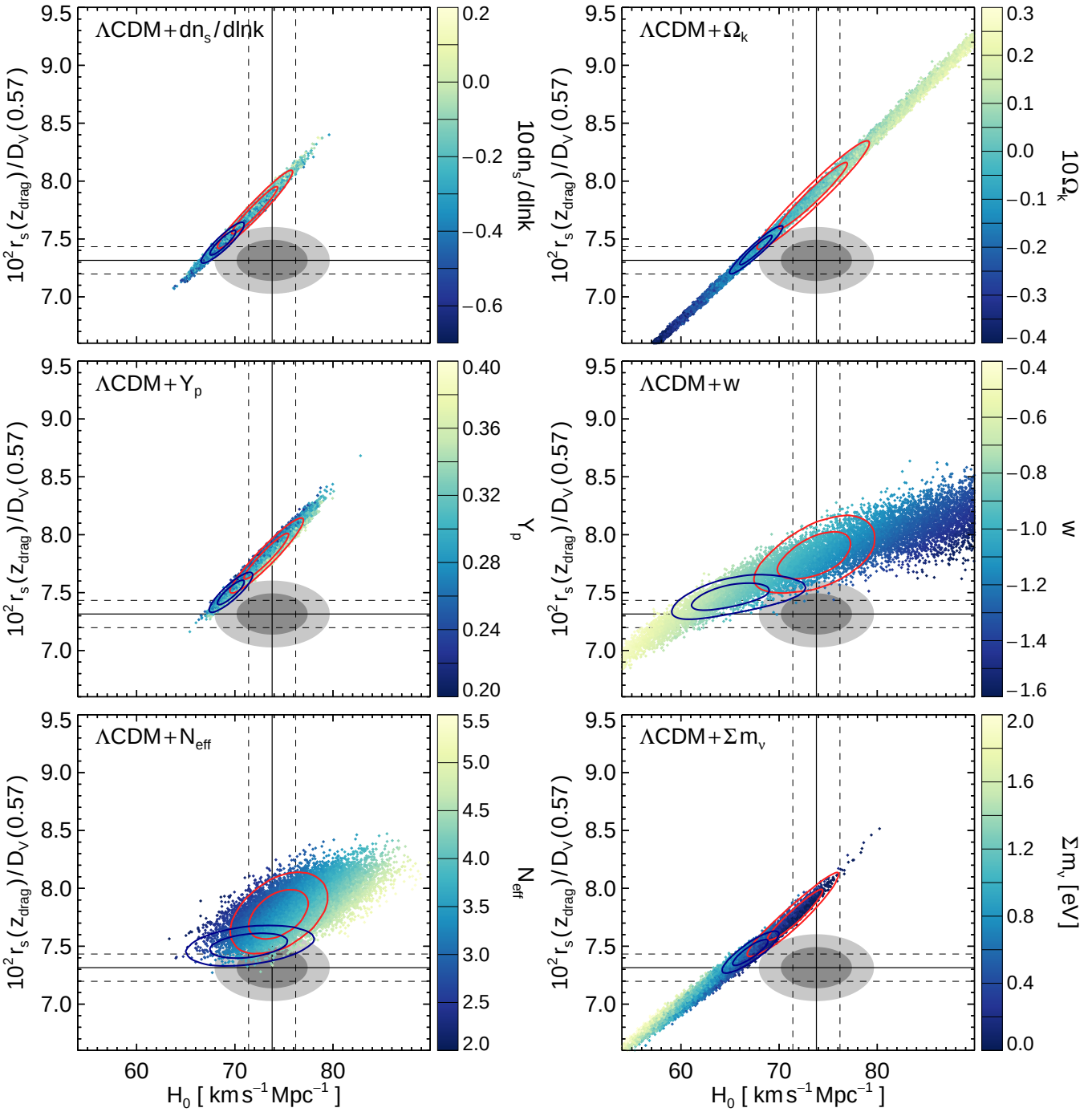

FIG. 4.— This figure expands Figure 3 to investigate the consistency between the CMB, $\mathrm{BAO_{BOSS}}$, and H_0 datasets in one-parameter extensions to ΛCDM. Each panel shows the $H_0 - r_s/D_V(0.57)$ plane for a different extension. The colored dots are samples drawn from the SPT+*WMAP*7 MCMC chain, with the color coding reflecting the value of the extension parameter, as shown in the color scales on the right. The horizontal solid and dashed lines mark the central value and $1\,\sigma$ region for the $\mathrm{BAO_{BOSS}}$ measurement, while the vertical lines do the same for H_0. The joint 1 and $2\,\sigma$ likelihood region for $\mathrm{BAO_{BOSS}}+H_0$ measurements is denoted by the dark and light grey shaded contours. The blue (red) contours overlaid show the 68% and 95% confidence regions for CMB+BAO (CMB+H_0). Varying the effective number of neutrino species leads to the best agreement between the CMB, $\mathrm{BAO_{BOSS}}$, and H_0.

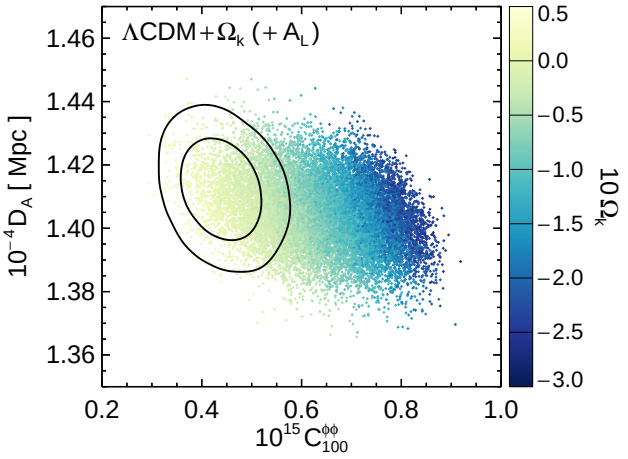

FIG. 5.— The impact of the angular diameter distance to last scattering, D_A, and the lensing information on the curvature constraint from the CMB. The contours show the 68% and 95% C.L. contours when lensing information is included. The colored points are samples from the posterior distribution after marginalzing over A_L, which effectively removes all lensing information. The allowed range of $C_{100}^{\phi\phi}$ values remains finite in the absence of lensing information, because the CMB still places (weaker) constraints on the ΛCDM+Ω_k model parameters. The color reflects the curvature value as indicated by the color bar on the right side of the plot. The lensing sensitivity of the data is clearly crucial to the curvature constraint from the CMB data.

the right column of Figure 4. Low-redshift datasets are especially important for constraining these extensions.

In summary, the CMB data prefer the $dn_s/d\ln k$ and Y_p extensions to ΛCDM because these extensions allow for an increasingly red tilt at higher multipoles. The preference for these two extensions remains in the CMB+BAO+H_0 combination. Although the quality of fit improves less for the ΛCDM+$N_{\rm eff}$ model, this model maximizes the consistency between the three datasets. The CMB+BAO+H_0 data also prefer the ΛCDM+$N_{\rm eff}$+$\sum m_\nu$ model, although this preference is less significant (given the 1 extra dof) than that for running. The three datasets are completely consistent within this two-parameter extension.

5. CURVATURE

The SPT+*WMAP*7 constraint on the mean curvature of the universe has been presented by Story et al. (2013). In brief, the addition of the SPT bandpowers tightens the *WMAP*7 constraint by a factor of five to $\Omega_k = -0.003^{+0.014}_{-0.018}$. Here we briefly present the physical underpinnings of how the SPT bandpowers tighten the constraint on Ω_k.

The constraint on curvature tightens due to the sensitivity of the SPT bandpowers to low-redshift information through gravitational lensing. S12 used the combination of SPT and *WMAP*7 bandpowers to report an $8.1\,\sigma$ detection of gravitational lensing of the CMB. Without the lensing information, the CMB constraints exhibit a strong degeneracy between curvature and the dark energy density. In essence, the primary CMB anisotropy is exquisitely sensitive to the angular-diameter distance to last scattering, but this is only one number. Therefore, if there are n parameters that only affect late-time geometry and structure, the CMB data will only tell us about one direction in this n-dimensional space. This is insufficient to distinguish between the two late-time parameters Ω_k and Ω_Λ. Lensing adds a second late-time measurement, breaking this degeneracy.

We demonstrate the effect of including lensing on curvature constraints from the CMB in Figure 5. The axes in the figure are the two late-time quantities constrained by the CMB data: the angular-diameter distance to last scattering, D_A, and the angular power spectrum of the lensing potential ϕ evaluated at $l = 100$, $C_{100}^{\phi\phi}$. The color-coded points are drawn from an SPT + *WMAP*7 MCMC chain with lensing information removed by marginalization over A_L.[31] We can see the impact of the geometric constraint, confining the samples to a narrow range of D_A values. Also, despite removing all lensing information, we see that the ΛCDM+Ω_k model predicts a finite range of values of the lensing power.

As Figure 5 shows, varying Ω_k leads to significant variation in the $C_{100}^{\phi\phi}$ direction in the $D_A - C_{100}^{\phi\phi}$ plane. The direction of the response in this plane is an important aspect of why lensing plays a significant role in constraining Ω_k whereas it does not for $\sum m_\nu$. The effect of lensing information (i.e., requiring $A_L = 1$) is shown by the black contours. The observed lensing amplitude rules out the negative curvature tail, and as mentioned above, tightens the curvature constraint from the CMB by a factor of five.

Better constraints on curvature are possible by including low-redshift probes. For instance, CMB+BAO+H_0 leads to a constraint on curvature of $\Omega_k = -0.0061 \pm 0.0040$. Even with low-redshift datasets included, SPT data remains important. Without the SPT bandpowers (and lensing information therein), the uncertainty would be roughly 15% larger: $\Omega_k = -0.0019 \pm 0.0047$ for *WMAP*7+BAO+H_0.

6. MASSIVE NEUTRINOS

We now consider allowing non-zero sum of neutrino masses. As we saw in § 4, the CMB data provide only a weak preference for this extension. However, once we include datasets sensitive to late times, the support for non-zero neutrino mass is fairly robust to the particular choice of the datasets and additional extensions of the ΛCDM model.

The range of possible neutrino masses is currently constrained from both above and below. Neutrino oscillation experiments place a lower bound on the sum of the neutrino masses of $\gtrsim 0.058\,$eV (Hamish Robertson 2009). Neutrino oscillations are insensitive to the sum of the neutrino masses above this minimum. The best laboratory upper bound on any single neutrino mass is $0.3 - 0.6\,$eV (90% CL) depending on the nuclear matrix elements adopted for the electron neutrino from the Kamland-Zen double beta decay experiment (Gando, et al. 2012). Therefore, the sum of the neutrino masses must lie between the limits $0.06\ \text{eV} < \sum m_\nu < 1.8\ \text{eV}$.

Cosmological observations can provide significantly stronger upper limits on the sum of the neutrino masses. The strongest constraints on $\sum m_\nu$ come from combining CMB measurements with low-redshift information.

[31] The current CMB data are insensitive to the small shape variations in $C_l^{\phi\phi}$ and hence marginalizing over a scaling parameter removes all significant lensing information.

TABLE 2
IMPROVEMENTS TO THE QUALITY OF FIT FOR EXTENSIONS TO THE ΛCDM MODEL

Dataset	ΛCDM $+dn_s/d\ln k$	ΛCDM $+N_{\rm eff}$	ΛCDM $+Y_p$	ΛCDM $+\sum m_\nu$	ΛCDM $+\Omega_k$	ΛCDM $+w$	ΛCDM $+N_{\rm eff}+\sum m_\nu$	ΛCDM $+N_{\rm eff}+Y_p$
CMB	4.9	1.1	4.4	2.4	0.3	0.0	2.6	5.5
CMB+BAO+H_0	7.4	3.4	5.3	2.8	2.0	0.2	7.9	5.4

This table shows how extensions to the ΛCDM model change the quality of the fit to the data for the CMB and the datasets combination of CMB+BAO+H_0. For each dataset we report $\Delta\chi^2$ defined as the reduction in χ^2 from the best-fit ΛCDM model to the best-fit ΛCDM+(extension) model. A large $\Delta\chi^2$ relative to the baseline ΛCDM model indicates that the extended model is a much better fit to the data. For instance, if $\Delta\chi^2 = 4$ (6.2) for a given extension with one (two) degrees of freedom, this means that the data favor this extension at $2\,\sigma$. Of the one-parameter model extensions considered here, both datasets have the strongest preference for non-zero running. Of the two-parameter model extensions considered here, the combined data prefer the ΛCDM+$N_{\rm eff}$+$\sum m_\nu$ model most strongly.

In this section, we include low-redshift measurements of the BAO feature, H_0, the halo power spectrum derived from SDSS luminous red galaxies (LRGs) from Reid et al. (2010), and the cluster abundances from the SPT SZ-selected cluster catalog ($\rm SPT_{CL}$) described by Reichardt et al. (2013). The LRG, H_0, and *WMAP*7 data have been used previously to set an upper limit on the neutrino masses of $\sum m_\nu < 0.44\,\rm eV$ (95% CL) (Komatsu et al. 2011). A somewhat tighter limit of $\sum m_\nu < 0.32\,\rm eV$ (95% CL) has been placed using SZ-selected galaxy clusters, CMB, BAO, and H_0 by Benson et al. (2013). Similar limits of about 0.3 eV come from combining CMB+BAO+H_0 with galaxy clustering data (Thomas et al. 2010; Riemer-Sørensen et al. 2012; de Putter et al. 2012) or X-ray cluster abundance and cluster gas mass fraction measurements (Mantz et al. 2010). As we note in § 6.2, the inclusion of the new BAO data (particularly the BOSS point) increases the preference for nonzero mass.

In this section, we present updated constraints on the sum of the neutrino masses incorporating the new SPT bandpowers. We first discuss how measurements of the CMB, structure growth, and geometry constrain massive neutrinos. We then present constraints for combinations of the SPT bandpowers and other datasets. We finally consider potential degeneracies between the sum of the neutrino masses and other parameter extensions such as running of the spectral index.

6.1. *Cosmological effects of massive neutrinos*

In this subsection, we give a physical description of the effects of the massive neutrinos on cosmology. We start with the effects massive neutrinos have on the CMB. We note that with the current experimental precision, information from CMB lensing is not important to the CMB constraints on $\sum m_\nu$. We then move on to consider other effects in the low-redshift universe.

To understand neutrino mass constraints from CMB data, we must understand how the predicted CMB power spectrum changes with neutrino mass. In the standard thermal history of the universe, massless neutrinos have a temperature corresponding to $\sim 0.17\,\rm eV$ at the epoch of last scattering. The scale at which masses start to have an appreciable effect is set by this temperature to be $\sum m_\nu \approx 3 \times 0.17\,\rm eV$.[32] Neutrino masses well below this value have no impact on primary CMB anisotropy. Hu & Dodelson (2002) and Ichikawa et al. (2005) study in detail the impact of higher masses on the CMB and find the dominant impact is due to the ISW effect.

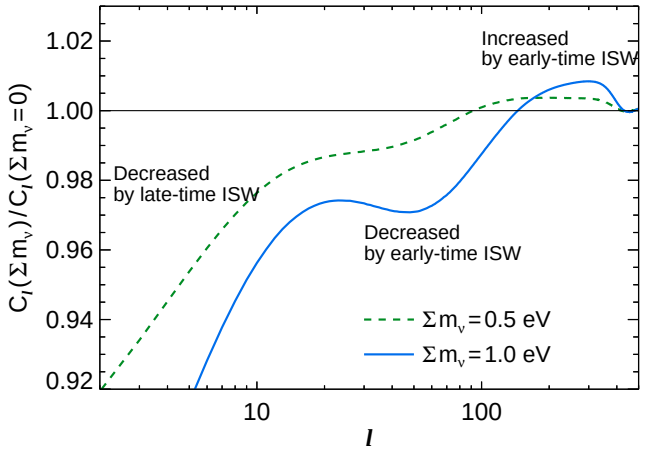

FIG. 6.— This figure shows the effects of massive neutrinos on the CMB power spectrum. The curves show the ratio of models with $\sum m_\nu = 0.5$ (**dashed green**) and 1.0 eV (**solid blue**) respectively to the best-fit ΛCDM ($\sum m_\nu$=0 eV) model spectrum for SPT+*WMAP*7. When increasing $\sum m_\nu$ we adjust Ω_Λ downward to keep θ_s fixed. On large scales, we see a reduction in the power added by the late-time ISW effect. On intermediate scales below the neutrino free-streaming length, we see a reduction in the power contributed by the early ISW effect. On scales smaller than the neutrino free-streaming length, the more rapid decay of gravitational potentials boosts the early ISW power. The amplitude of the early ISW effect is damped at $l \gtrsim 500$ by averaging over multiple positive and negative contributions.

In a matter-dominated universe with zero mean curvature, gravitational potentials remain constant to first order in linear perturbation theory. Adding components that do not cluster, while keeping the curvature fixed to zero, increases the expansion rate which causes the gravitational potentials to decay. As photons traverse these decaying potentials on their way toward the observer, new anisotropies are created by what is called the Integrated Sachs-Wolfe (ISW) effect. The ISW anisotropy is generated in the ΛCDM model both at early times, as photons free stream immediately after decoupling through a not-completely-matter-dominated universe (the early ISW effect) and at late times after the cosmological constant becomes important (the late ISW effect).

We illustrate how the ISW effect changes with neutrino

[32] For simplicity we assume three families of neutrinos with degenerate masses.

mass in Figure 6. In this figure, we plot the ratio of C_l at either $\sum m_\nu = 0.5$ or 1.0 eV relative to a fiducial ΛCDM+$\sum m_\nu$ model $C_l^{\rm fid}$ with $\sum m_\nu = 0.0$. The baryon density ω_b, cold dark matter density ω_c, and the sound horizon scale θ_s are fixed between the three models – $\sum m_\nu$ and Ω_Λ vary. Three regimes are labeled in the figure: a reduction of power due to the late-time ISW effect at $l \lesssim 20$, a reduction of power due to the early ISW effect at $20 \lesssim l \lesssim 100$, and an increase in power due to the early ISW effect at $100 \lesssim l \lesssim 500$. We briefly explain these three regimes in the next paragraphs.

As $\sum m_\nu$ increases with $\omega_b + \omega_c$ fixed, the expansion rate increases at early times. Therefore, Ω_Λ must decrease (increasing D_A) to keep θ_s fixed. Without this adjustment to Ω_Λ, θ_s would change, primarily due to the change in D_A. With this adjustment, we find that in the mass range of interest, $H(z)$ increases relative to the $\sum m_\nu = 0$ model at $z \gtrsim 1$ and decreases at $z \lesssim 1$. The decreased expansion rate at $z \lesssim 1$ results in less decay of the gravitational potential on very large scales, and therefore a reduction in the contribution to the power from the late-time ISW effect. The net effect is less power at $l \lesssim 20$. However, the large cosmic variance at these low multipoles makes the CMB data largely insensitive to the reduced power.

On scales shorter than the neutrino free-streaming length, the increased expansion rate just after photon decoupling enhances the decay of gravitational potentials and thus enhances the early ISW effect. On scales longer than the free-streaming length, the early ISW effect is suppressed; the clustering of neutrinos prevents the potential from decaying more rapidly and, due to the increased expansion rate, there is less time for the early ISW effect to accumulate. The dividing line in multipole space between these two regimes increases with $\sum m_\nu$. The magnitude of the ISW effect decreases with increasing l as cancellations between an increasing number of positive and negative contributions washes out the signal, becoming negligible by $l \sim 500$.

The reduction of power at $l \lesssim 100$ and increase of power at $l \gtrsim 100$ shown in Figure 6 can be mimicked by an increase in ω_b and n_s. As a result, $\sum m_\nu$ is anti-correlated with ω_b and n_s. Figure 7 shows this anti-correlation between $\sum m_\nu$ and n_s.

Although the ISW effect is limited to angular scales covered by *WMAP*, SPT bandpowers contribute significantly to the neutrino mass constraints by alleviating these degeneracies between $\sum m_\nu$, n_s, and ω_b. In particular, SPT alone prefers a lower value of n_s relative to *WMAP*7 (see Figure 2), which causes the preferred value of $\sum m_\nu$ to increase when SPT data are combined with *WMAP*7. This shift in the SPT-preferred value of n_s disappears with a freely varying Y_p or $dn_s/d\ln k$, thus the shift in $\sum m_\nu$ for the combination of SPT+*WMAP*7 disappears as well when these parameters are added. These shifts in the preferred value of $\sum m_\nu$ are seen clearly in Figure 8.

Next, we examine the other observable consequences that massive neutrinos have on the geometry and the growth of structure at late times. The decreased expansion rate at $z \lesssim 1$ directly affects the late-time geometry, and geometric observables. BAO measurements constrain the late-time expansion rate through

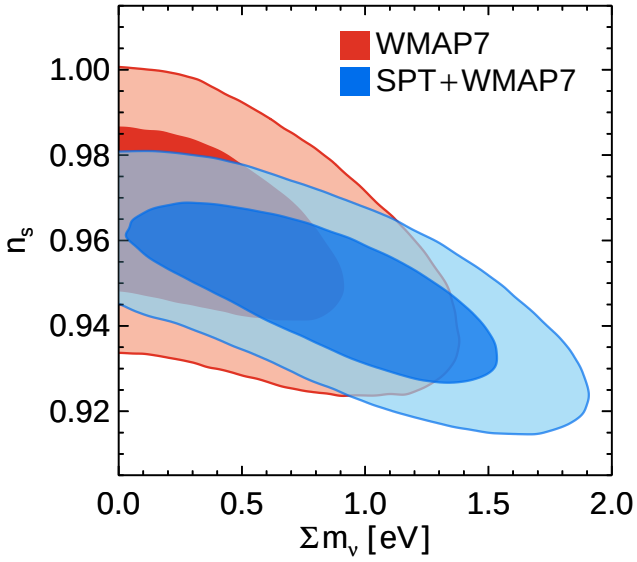

FIG. 7.— This figure illustrates the degeneracy between n_s and $\sum m_\nu$, and its role in the SPT+*WMAP*7 preference for nonzero neutrino masses. The contours are the 68% and 95% confidence intervals in the ΛCDM+$\sum m_\nu$ parameter space for *WMAP*7 (red) and SPT+*WMAP*7 (blue). The SPT data prefer a lower value of n_s than *WMAP*7, which leads the CMB data to prefer higher $\sum m_\nu$.

$r_s(z_{\rm drag})/D_V(z)$. Although increasing $\sum m_\nu$ from zero to 1.5 eV has some effect on $r_s(z_{\rm drag})$, the dominant effect is the increase in $D_V(z)$ as Ω_Λ decreases. Therefore $r_s(z_{\rm drag})/D_V(z)$ and H_0 respond similarly, decreasing with increasing neutrino mass as shown in Figure 9.

For $z \gtrsim 1$, the increased expansion rate suppresses growth on scales below the neutrino free-streaming length (~ 140 Mpc for a 100 meV neutrino). On larger scales the neutrinos can cluster, which counteracts the suppression. For $z \lesssim 1$, the reduced expansion rate boosts the rate of structure growth on all scales. We hasten to point out, though, that the net effect on integrated growth to $z = 0$ on small scales is that of suppression.

In summary, the summed neutrino mass is constrained by the CMB primarily through the early ISW effect. The SPT data improve $\sum m_\nu$ constraints indirectly via an improved determination of n_s and the anti-correlation of $\sum m_\nu$ with n_s. Adding probes of low-redshift geometry and structure growth further improve constraints on $\sum m_\nu$. We discuss these constraints in the next section.

6.2. *Cosmological constraints on massive neutrinos*

We now look at the cosmological constraints on neutrino mass. In order to discuss changes in the posterior probability density for $\sum m_\nu$ near the prior at zero, we will sometimes quote a different confidence interval than the rest of the paper. In Table 3 and this section, we report the estimated confidence interval $\sum m_\nu \in [x_1, x_2]$ (68% CL) such that

$$\int_{x_1}^{x_2} P(\sum m_\nu) d(\sum m_\nu) = 0.68, \qquad (5)$$

where $P(x_1) = P(x_2)$ and $P(\sum m_\nu)$ is the normalized neutrino mass posterior probability density. When we find $P(0) > P(x_2)$, we report the confidence interval as $[0, x_2]$; this is an upper limit. We will also report the peak

TABLE 3
ΛCDM+$\sum m_\nu$ RESULTS FROM VARIOUS COMBINATIONS OF DATASETS

Datasets Combinations	$\sum m_\nu$ [eV] 68% CL	$\sum m_\nu$ [eV] 95% CL	Peak	$10^2\Omega_b h^2$	n_s	H_0 [km s^{-1} Mpc^{-1}]	σ_8
CMB	[0.41, 1.34]	[0, 1.60]	0.93	2.184 ± 0.041	0.948 ± 0.014	$62.8^{+5.3}_{-4.0}$	$0.658^{+0.075}_{-0.061}$
CMB+BAO	[0.29, 0.68]	[0.11, 0.88]	0.48	2.207 ± 0.034	0.957 ± 0.008	67.1 ± 1.2	0.712 ± 0.048
CMB+H_0	[0, 0.24]	[0, 0.48]	0.01	2.233 ± 0.035	0.965 ± 0.009	71.6 ± 1.8	$0.758^{+0.031}_{-0.039}$
CMB+LRG	[0.17, 0.61]	[0, 0.78]	0.39	2.204 ± 0.036	0.956 ± 0.009	66.4 ± 2.5	0.731 ± 0.048
CMB+SPT$_{\rm CL}$	[0.28, 0.80]	[0, 1.03]	0.55	2.196 ± 0.040	0.954 ± 0.011	$65.1^{+3.8}_{-3.4}$	$0.702^{+0.045}_{-0.038}$
CMB+BAO+H_0	[0.16, 0.51]	[0, 0.66]	0.33	2.219 ± 0.034	0.959 ± 0.008	68.4 ± 1.0	0.741 ± 0.046
CMB+BAO+H_0+ SPT$_{\rm CL}$	[0.21, 0.43]	[0.10, 0.54]	0.32	2.221 ± 0.034	0.960 ± 0.008	68.3 ± 1.0	0.739 ± 0.027

This table shows the results for the ΛCDM+ $\sum m_\nu$ model. The confidence level intervals shown indicate the region of highest probability density that contains either 68% or 95% of the probability. The 'Peak' value is the peak of the posterior distribution. We include some other parameters of particular interest for this extension. Note in particular that high peak values of $\sum m_\nu$ correspond to low values of n_s, low values of H_0 and low values of σ_8.

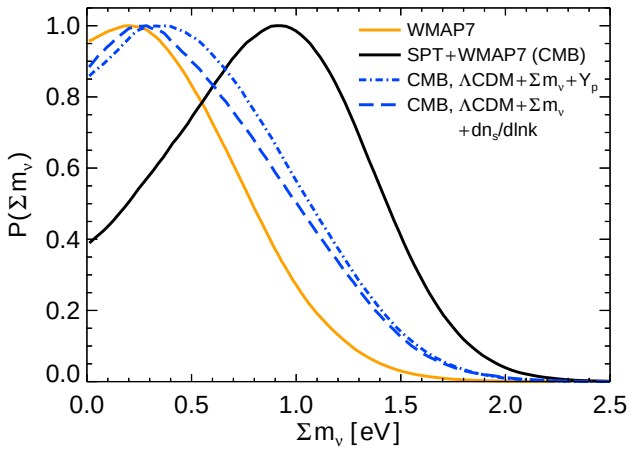

FIG. 8.— The constraints on $\sum m_\nu$ from the CMB data degrade significantly when we decouple the tilt of the primordial power spectrum on small and large scales. The marginalized one-dimensional posteriors of $\sum m_\nu$ from *WMAP*7 (SPT+*WMAP*7) data are shown with the orange solid (black solid) line. The SPT data prefer a lower value of n_s than *WMAP*7, which leads the CMB data to prefer higher $\sum m_\nu$. If the tilt of the primordial power law on small and large scales is decoupled, whether directly by introducing running (blue dashed line) or indirectly by freeing the damping scale with the introduction of Y_p (blue dot-dashed line), the shift towards higher neutrino masses in the CMB likelihood is substantially reduced.

of $P(\sum m_\nu)$. For cases with a non-zero 95% confidence lower limit as defined above, we will continue to report the median and $1\,\sigma$ error which is used in the rest of the paper and defined in § 2.3.

The SPT data prefer lower values of n_s than those preferred by *WMAP*7, which translates into a preference for higher neutrino masses. For the SPT+*WMAP*7 data, we find the position of the peak moves to 0.93 eV with a 68% confidence interval of $\sum m_\nu \in [0.41, 1.34]$ eV. The 95% CL upper limit from the CMB is $\sum m_\nu < 1.60$ eV.

We now consider low-redshift probes of geometry: BAO and H_0. As mentioned above, these low-redshift geometric probes can strengthen inferences of neutrino mass through the impact on the expansion rate. With massive neutrinos, the CMB data is compatible with either the BAO or H_0 measurements (see Figures 4 and 9), though the resulting constraints on $\sum m_\nu$ are quite different. Adding BAO data to the CMB data tightens the neutrino mass constraint significantly; for the combination of CMB+BAO, we obtain a $2.4\,\sigma$ preference for nonzero neutrino masses with $\sum m_\nu = (0.49 \pm 0.20)$ eV. The 95% confidence interval is $\sum m_\nu \in [0.11, 0.88]$ eV. On the other hand, the H_0 dataset prefers higher values of H_0, corresponding to lower values of $\sum m_\nu$. The likelihood for CMB+H_0 peaks near zero neutrino mass, with an upper limit of $\sum m_\nu < 0.48$ eV (95% CL). Combining all three datasets produces a neutrino mass constraint that lies between the CMB+BAO and CMB+H_0 constraints. For the combination of CMB+BAO+H_0, we find the posterior peaks at 0.33 eV with a 68% confidence interval of $\sum m_\nu \in [0.16, 0.51]$ eV. The 95% CL upper limit is $\sum m_\nu < 0.66$ eV. The constraints from these combinations are shown in Figure 10. As an aside, we note that as in the CMB-only case, the small-scale information from SPT data is a significant contributor to the suggestion of nonzero neutrino masses. Without the SPT bandpowers, the neutrino mass probability density for *WMAP*7+BAO+H_0 peaks just above zero mass with a 95% CL upper limit of $\sum m_\nu < 0.48$ eV.

We next turn to low-redshift probes of structure growth: LRGs and galaxy clusters. For the CMB+LRG dataset, we find the posterior probability peaks at 0.39 eV with a 68% confidence interval of $\sum m_\nu \in [0.17, 0.61]$ eV. The 95% confidence interval is an upper limit at $\sum m_\nu < 0.78$ eV (95% CL). Instead, adding the SPT galaxy cluster sample[33] (SPT$_{\rm CL}$) to the CMB leads the posterior probability to peak at slightly higher masses 0.55 eV with a 68% confidence interval of $\sum m_\nu \in [0.28, 0.80]$ eV. The 95% CL upper limit is $\sum m_\nu < 1.03$ eV. Both the CMB+LRG and CMB+SPT$_{\rm CL}$ combinations show a preference for non-zero neutrino mass at just under $2\,\sigma$.

Finally, we combine the CMB, geometrical, and large-scale structure observations. Because the SDSS LRG and SDSS BAO galaxy samples overlap, we do not include the LRG dataset in this combination. In this case, we find (for CMB+BAO+H_0+SPT$_{\rm CL}$):

$$\sum m_\nu = (0.32 \pm 0.11)\,\text{eV}, \qquad (6)$$

[33] Note that the interpretation of the measured galaxy number counts depends on the Tinker mass function (Tinker et al. 2008). Although the Tinker mass function was not originally calculated for massive neutrinos, later papers (Marulli et al. 2011; Ichiki & Takada 2012) have shown that if rescaled to the new value of σ_8, the Tinker mass function remains accurate for massive clusters ($M > 10^{14} h^{-1} M_\odot$) – which includes all SPT galaxy clusters.

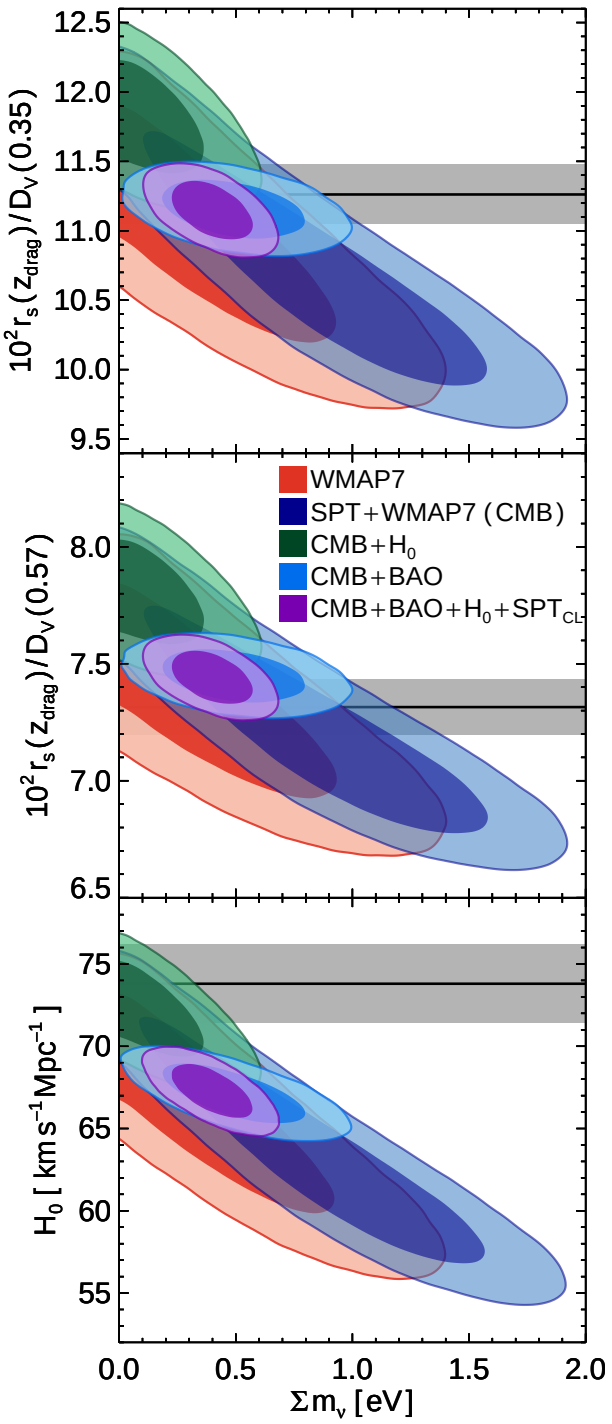

FIG. 9.— This figure shows how low-redshift datasets affect the neutrino mass constraints. In the planes of $\sum m_\nu$ and three quantities inferred at low redshifts, we show the marginalized two-dimensional posteriors from different combinations of datasets shown by the legend in the central panel. *Top*: constraints are plotted in the $\sum m_\nu - r_s(z_{\rm drag})/D_V(0.35)$ plane with the SDSS BAO data point shown by the grey band as the $1\,\sigma$ region. *Middle*: similar to the left panel but showing $r_s(z_{\rm drag})/D_V(0.57)$ with the BOSS BAO data point for the gray band as the $1\,\sigma$ region. *Bottom*: similar to the top and middle panels but showing H_0 with the grey band showing the $1\,\sigma$ region. The tension between BAO and H_0 can be seen in the three panels. The CMB+BAO preference for massive neutrinos is clearly visible.

$$\sum m_\nu \in [0.01, 0.63]\,{\rm eV}\ (99.7\%\,{\rm CL})\,. \qquad (7)$$

This data combination gives a $3\,\sigma$ preference for positive neutrino masses. Without BAO, the preferred mass drops significantly while the uncertainties increase; the constraint is consistent with no mass at 68% confidence, and we end up with an upper limit of $\sum m_\nu < 0.39\,{\rm eV}\,(95\%\,{\rm CL})$. Without H_0, the likelihood shifts to higher masses without degrading the uncertainties, $\sum m_\nu = (0.40 \pm 0.11)\,{\rm eV}$.

The are several drivers behind the $\sum m_\nu$ constraint (Equation 6) derived from the dataset combination of CMB+BAO+H_0+SPT$_{\rm CL}$:

- CMB: As discussed above, the CMB data contribute to this constraint by enforcing the height of the first and second acoustic peaks (from *WMAP*7 data) and the slope of the damping tail (from SPT data). The latter leads to a lower n_s, with $\sum m_\nu$ thus increasing to compensate for the changes to the power in the *WMAP*7 region. The resulting posterior distribution from the CMB peaks around $\sum m_\nu \sim 1\,{\rm eV}$. These CMB constraints contribute $\sim 1\,\sigma$ to the combined $\sum m_\nu$ constraint. If we keep only the optical depth prior from *WMAP*7, we find a confidence interval of $\sum m_\nu \in [0.07, 0.53]\,{\rm eV}$ (95% CL). Without the SPT bandpowers (and n_s information), the confidence interval is $\sum m_\nu \in [0.03, 0.48]\,{\rm eV}$ (95% CL). In both cases, there remains a greater than $2\,\sigma$ preference for nonzero masses.

- BAO: The BAO measurement is an important driver of the combined neutrino mass constraint. As seen in Figure 10, the BAO measurements push up the preferred value of $\sum m_\nu$ and tighten the constraints considerably relative to the other datasets. The preference for massive neutrinos is common between the three BAO datasets. To confirm the robustness of the BAO preference, we have run three MCMC chains, dropping one of the BAO datasets in each chain. When dropping the SDSS, WiggleZ, or BOSS dataset, we find, at 95% CL, $\sum m_\nu \in [0.10, 0.55]$, $[0.10, 0.53]$, or $[0.03, 0.47]\,{\rm eV}$ respectively. In short, the BAO data prefer massive neutrinos, and the results are robust against dropping any single BAO observation. The largest shift of $0.6\,\sigma$ is introduced by dropping the BOSS measurement. However as previously noted, if all BAO measurements are removed and H_0 information is included, the preference for massive neutrinos disappears.

- SPT$_{\rm CL}$: Adding the SPT$_{\rm CL}$ galaxy cluster sample reduces the neutrino mass uncertainties by a factor of 1.6 without significantly changing the median value, as can be seen by comparing the value without clusters – $\sum m_\nu = (0.34 \pm 0.18)\,{\rm eV}$ – to the value with clusters – $\sum m_\nu = (0.32 \pm 0.11)\,{\rm eV}$. In principle, this result depends on the accuracy of the cluster mass calibration, which was determined through an X-ray based scaling relation. To test this dependency, we have doubled the uncertainty on the normalization of the X-ray scaling relation and find little change in the distribution,

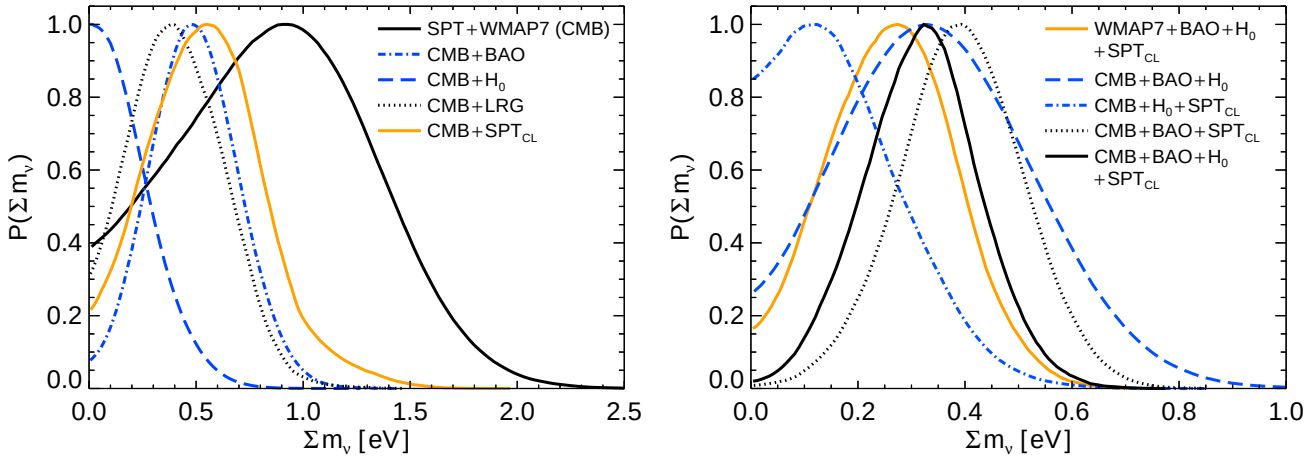

FIG. 10.— ***Left panel:*** This panel demonstrates how the marginalized one-dimensional posterior distribution of $\sum m_\nu$ changes when a single external dataset is *added* to the CMB dataset. The CMB constraint is shown by the black solid line. The datasets added are the BAO data (blue dot-dashed line), H_0 measurement (blue dashed line), LRG sample (black dotted line), and SPT cluster data (orange solid line). ***Right panel:*** This panel demonstrates how the marginalized one-dimensional posterior distribution of $\sum m_\nu$ changes when a single external dataset is *removed* from the combination of CMB+BAO+H_0+SPT$_{\rm CL}$. The datasets dropped are the SPT bandpowers (orange solid line), SPT$_{\rm CL}$ (blue dashed line), BAO data (blue dot-dashed line), and H_0 measurement (black dotted line). The marginalized posterior for the combined CMB+BAO+H_0+SPT$_{\rm CL}$ dataset is shown by the black solid line.

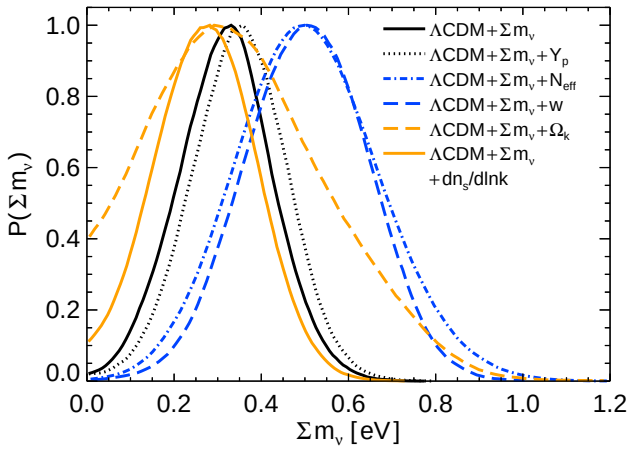

FIG. 11.— This figure illustrates the robustness of the preference for positive neutrino masses to other parameter extensions. The marginalized one-dimensional posteriors for $\sum m_\nu$ are shown for two-parameter extensions to ΛCDM for the combined CMB+BAO+H_0+SPT$_{\rm CL}$ data sets (for w, SNe are used instead of H_0). Allowing significant curvature or running can significantly reduce the preference for nonzero neutrino masses (to 1.7 and 2.4 σ respectively). Other extensions increase the preference for positive neutrino masses.

$\sum m_\nu = (0.34 \pm 0.12)$ eV. We conclude that the reduction in uncertainties is insensitive to the specific prior on the mass scaling relation.

As shown in Table 3, allowing for non-zero neutrino masses decreases the value of σ_8 inferred by the SPT and *WMAP7* ($\sigma_8 = 0.658^{+0.075}_{-0.061}$) from the value obtained within the ΛCDM model ($\sigma_8 = 0.795 \pm 0.022$) by roughly 2σ. Inferring σ_8 from the CMB is quite indirect, and allowing for neutrino masses introduces a large degeneracy which, when compared to ΛCDM, significantly enlarges the uncertainty on σ_8. The preference for positive neutrino mass discussed above shifts the median of σ_8 down. Within the ΛCDM + $\sum m_\nu$ model, the constraints from adding SPT data are consistent with the constraints inferred from *WMAP7* alone, $\sigma_8 = 0.685^{+0.079}_{-0.078}$ (Komatsu et al. 2011). This is also consistent with the low redshift probe on σ_8. For example, the constraint on the quantity $\sigma_8(\Omega_m/0.25)^{0.47}$ from X-ray clusters gives $\sigma_8(\Omega_m/0.25)^{0.47} = 0.813 \pm 0.013\,({\rm stat}) \pm 0.024\,({\rm sys})$ (Vikhlinin et al. 2009), and $\sigma_8(\Omega_m/0.25)^{0.47} = 0.785 \pm 0.050$ from CMB within the same model - consistent at $0.5\,\sigma$.

We conclude that the preference for nonzero neutrino masses is coming from three independent sources and remains at $> 2\,\sigma$ significance as long as we keep cluster abundances and at least one of the two most precise BAO measurements.

6.3. *Degeneracies with other extensions*

A final question is to what extent the neutrino mass constraint is weakened by introducing additional free parameters to the 7-parameter ΛCDM+$\sum m_\nu$ model. To address this, we show the marginalized posteriors for the sum of the neutrino masses in 8-parameter models in Figure 11. We consider several possible additions: Y_p, $N_{\rm eff}$, $dn_s/d\ln k$, Ω_k, or w. All curves are for the combination of CMB+BAO+H_0+SPT$_{\rm CL}$.

Of these five extensions, two ($dn_s/d\ln k$ and Ω_k) decrease the preference for positive $\sum m_\nu$, two (w and $N_{\rm eff}$) increase the preference, and one (Y_p) has minimal effect. Allowing both curvature and massive neutrinos significantly increases the uncertainties on both parameters. The peak of the neutrino mass likelihood remains nearly unchanged at 0.34 eV with the 95% confidence interval expanded to $\sum m_\nu \in [0, 0.70]$ eV. The curvature is consistent with zero. Allowing for running of the spectral index reduces the preference for nonzero neutrino masses, in this case by shifting the median down; the neutrino mass constraint with running is $\sum m_\nu = (0.27 \pm 0.11)$ eV. On the other hand, allowing the dark energy equation of state or number of neutrino species to vary increases the preference for positive neutrino masses. The summed neutrino mass is correlated with $N_{\rm eff}$ (see § 9.2 and Ichikawa et al. 2005) and anti-correlated with w (Zhao et al. 2012). Freeing either of these parameters increases the median masses, although the uncertainties also increase. For a wCDM+$\sum m_\nu$ model, the mass constraint

is $\sum m_\nu = (0.51 \pm 0.14)\,\mathrm{eV}$, $3.7\,\sigma$ above zero. For a ΛCDM+$N_{\rm eff}$+$\sum m_\nu$ cosmology, the mass constraint is $\sum m_\nu = (0.51 \pm 0.15)\,\mathrm{eV}$. This last case is discussed in detail in § 9.2. We find the CMB+BAO+H_0+SPT$_{\rm CL}$ preference for neutrinos remains at greater than 95% confidence when we add additional model parameters, with the exception of the mean curvature of the universe. Fitting the posterior with a Gaussian, we find curvature reduces the preference for massive neutrinos to $1.7\,\sigma$.

7. RUNNING OF THE SPECTRAL INDEX

The difference in preferred n_s from SPT and *WMAP*7 data suggests a scale dependence in the power spectrum of the primordial fluctuations. To test this, we allow the primordial power spectrum to deviate from a pure power law by introducing a logarithmic dependence on scale k, a so-called "running spectral index" (Kosowsky & Turner 1995):

$$n_s(k) = n_s(k_0) + dn_s/d\ln k \ln\left(\frac{k}{k_0}\right). \quad (8)$$

Here, k_0 is a defined pivot point and $dn_s/d\ln k$ is the running parameter. Throughout this section, we will define this pivot point to be $k_0 = 0.025\,\mathrm{Mpc}^{-1}$, which projects to $l \simeq 350$. This pivot point is chosen to decorrelate the uncertainties on n_s and $dn_s/d\ln k$ in the SPT+*WMAP*7 data.

The running parameter $dn_s/d\ln k$ is predicted to be undetectable by most inflationary theories, and a detection of non-zero $dn_s/d\ln k$ could provide information about the inflationary potential (Kosowsky & Turner 1995), or point to models other than inflation. There have been a number of recent CMB constraints on running. Komatsu et al. (2011) obtain $-0.084 < dn_s/d\ln k < 0.020\,(95\%\,\mathrm{CL})$ from *WMAP*7. Dunkley et al. (2011) find $dn_s/d\ln k = -0.034 \pm 0.018$ from *WMAP*7+ACT. K11 use the combination of *WMAP*7 data and the first 790 deg^2 SPT survey data to obtain $dn_s/d\ln k = -0.024 \pm 0.013$, a preference for negative spectral running at $1.8\,\sigma$.

7.1. *Constraints on $dn_s/d\ln k$*

We now look at the constraints on $dn_s/d\ln k$ from the SPT bandpowers. As shown in the left panel of Figure 12, adding the SPT bandpowers to *WMAP*7 dramatically reduces the allowed likelihood volume, and leads to a preference for negative running. For SPT+*WMAP*7, we find:

$$dn_s/d\ln k = -0.024 \pm 0.011. \quad (9)$$

The probability of negative running with the CMB data is $P(dn_s/d\ln k \leq 0) = 98.6\%$, equivalent to a $2.2\,\sigma$ Gaussian preference. In the appendix, we examine the dependence of the preference for negative running on the multipole range, and beam or foreground priors. We conclude that the preference does not depend strongly on the SPT experimental beam uncertainty or foreground modeling.

Adding BAO and H_0 data marginally improves the constraints and shifts the median to more negative values. The combination CMB+BAO+H_0 constrains $dn_s/d\ln k$ to be

$$dn_s/d\ln k = -0.028 \pm 0.010. \quad (10)$$

The small shift from the CMB constraint is driven almost entirely by the BAO data, which prefers smaller values of H_0. The probability of negative running with the CMB+BAO+H_0 data is $P(dn_s/d\ln k \leq 0) = 99.7\%$, equivalent to a $2.7\,\sigma$ Gaussian preference.

We next consider how robust the preference for negative running is to other model extensions. Introducing tensor perturbations (by making the tensor-to-scalar ratio r a free parameter) is a particularly natural extension in the context of inflationary models. However, the preference for running cannot be reduced by non-zero tensor perturbations. Tensor modes would increase the power at large scales without affecting small and intermediate scales. Adding tensor modes, therefore, increases the preference for negative running. In a ΛCDM+r+$dn_s/d\ln k$ cosmology, we obtain $dn_s/d\ln k = -0.045 \pm 0.016$ for the CMB data and $dn_s/d\ln k = -0.046 \pm 0.015$ for the CMB+BAO+H_0.

More generally, the preference for negative running might be reduced by any extension that also effectively allows for an increasingly red, scale-dependent tilt. We thus consider how the running constraint changes for the CMB data alone when freeing $\sum m_\nu$, $N_{\rm eff}$, or Y_p. For $dn_s/d\ln k$ +$\sum m_\nu$, we find $dn_s/d\ln k = -0.020 \pm 0.012$, similar to the $\sum m_\nu = 0\,\mathrm{eV}$ constraint of $dn_s/d\ln k = -0.024 \pm 0.011$. For $dn_s/d\ln k$ +$N_{\rm eff}$, we find a shift to more negative running and larger uncertainties, $dn_s/d\ln k = -0.034 \pm 0.017$. We find the largest increase in the uncertainties for $dn_s/d\ln k$ +Y_p, $dn_s/d\ln k = -0.020 \pm 0.024$. Therefore, the significance of the preference for running is most reduced by freeing Y_p and, to a lesser extent, $N_{\rm eff}$, and we plot constraints for these extensions in the right panel of Fig. 12 as well as Fig. 13.

As will be discussed in § 8, the primary effect of Y_p and $N_{\rm eff}$ is on the damping scale – which obviously mimics running. This degeneracy expands the uncertainty on $dn_s/d\ln k$. The shift in the ISW effect due to massive neutrinos does not mimic the scale dependence of running very well and has minimal effect. Freeing $N_{\rm eff}$ and Y_p yield different results because, as will be discussed in § 9, $N_{\rm eff}$ also changes the locations of the acoustic peaks – which running and Y_p do not. This reduces the degeneracy between the parameters and also explains the shift in the preferred value for running. With $dn_s/d\ln k$ +$N_{\rm eff}$ free, the model is free to move to lower values of $N_{\rm eff}$ to better match the observed peak locations while compensating for the decreased damping with negative running.

Among the models considered, the preference for negative running is only removed by freeing the helium abundance. However, the inferred helium abundance is in tension with the $2\,\sigma$ upper limit of the protosolar measurement that will be discussed in § 8.2. Forcing Y_p to be less than this $2\,\sigma$ upper limit of $Y_p < 0.294$ degrades the effectiveness of Y_p in removing the preference for negative running. This point is illustrated by the purple contours in the right panel of Figure 12 and the blue dot-dashed line in Figure 13. Excluding values of Y_p above 0.294, the preference for running is robust against other model extensions.

7.2. *Implications for Inflationary Models*

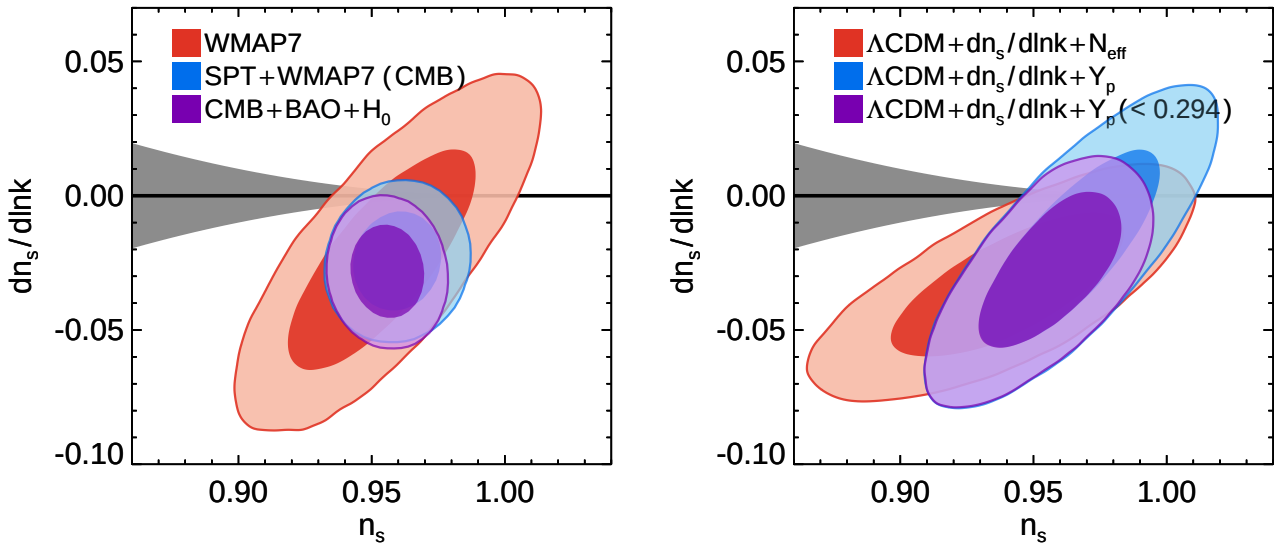

FIG. 12.— The data prefer negative running; this preference remains when additional parameters are freed. We show the marginalized two-dimensional posteriors for n_s (at $k = 0.025$ Mpc^{-1}) and $dn_s/d\ln k$. ***Left panel:*** the n_s- $dn_s/d\ln k$ joint distribution in the ΛCDM+$dn_s/d\ln k$ model for different combinations of the datasets. ***Right panel:*** the n_s- $dn_s/d\ln k$ joint distribution obtained by marginalizing $N_{\rm eff}$ (red) and Y_p (blue) for *WMAP*7+SPT data. The purple filled contours show the case with Y_p marginalized with the prior $Y_p < 0.294$, the $2\,\sigma$ upper limit of the solar initial helium abundance by Serenelli & Basu (2010). We show the region where $|dn_s/d\ln k| < (1-n_s)^2$ in gray. Inflation models with slow-roll expansion that can be terminated at second order make predictions in this region.

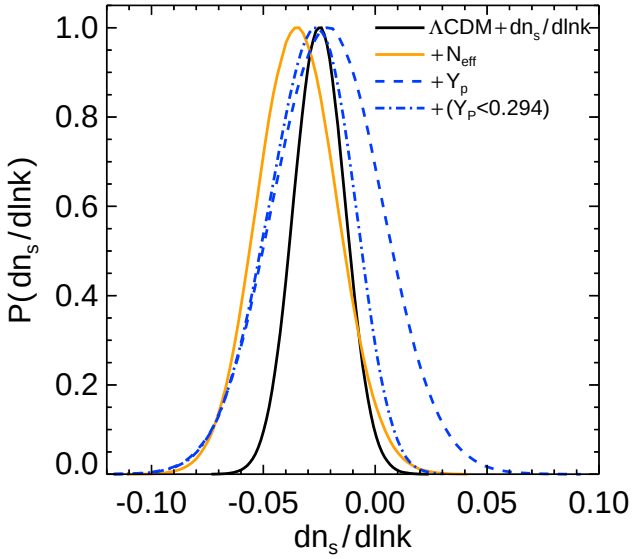

FIG. 13.— The preference of the SPT+*WMAP*7 data for negative running remains as additional parameters are freed. The marginalized one-dimensional posteriors for $dn_s/d\ln k$ from the CMB in the ΛCDM+$dn_s/d\ln k$ model is shown by the black solid line. The preference for negative running is reduced when $Y_{\rm p}$ is allowed to vary (blue dashed line), although this depends on extremely high helium abundances. If an upper limit based on solar abundances is set on Y_p, the preference for negative running is mostly restored (blue dot-dashed line). Allowing $N_{\rm eff}$ to vary (orange solid line) increases the preference for negative running.

We now explore the implications of the constraint on running for models of inflation. Although we expect n_s to have some scale dependence, $dn_s/d\ln k$ is predicted to be undetectably small with current data in single-field, slow-roll inflation models. These models predict $dn_s/d\ln k$ to be second order in the slow roll parameters, and thus of order $(1-n_s)^2$ unless the potential experiences significant jerk in the observable range (Chung et al. 2003; Finelli et al. 2010). A significant detection of running is a potential problem for both small and large-field inflation models. Small-field inflation models predict $r \simeq 0$, thus one can interpret the n_s–$dn_s/d\ln k$ constraints shown in Figure 12 as a direct test of small-field models. The observed value of $dn_s/d\ln k$ disfavors single-field small-field inflation with negligible jerk at the $\sim 2\,\sigma$ level ($\sim 2.7\,\sigma$ for CMB+BAO+H_0). Large-field inflation models, which predict non-negligible r (and thus more negative running), are even more disfavored.

Models with significant jerk at observable scales can allow for larger absolute values of running (Easther & Peiris 2006), however for $n_s \lesssim 1$, these models also predict a number of e-foldings $N \lesssim 30$.[34] Here e^N gives the increase in the scale factor between the time when the observable scale leaves the horizon and the end of inflation. Such small values of N are incompatible with a standard cosmological history (Liddle & Leach 2003), as they imply an energy scale of inflation which is below the electroweak phase transition (Easther & Peiris 2006). We therefore treat the prediction that $dn_s/d\ln k$ is of order $(1-n_s)^2$ as a fairly robust one for single-field slow-roll models.

Finally, we mention that the choice of a constant $dn_s/d\ln k$ as a departure from power law behavior in the primordial spectrum is not the only possible choice. It is also possible that the running is significant over only a small range of wavenumber k; Cline & Hoi (2006) argue that such a parametrization fits more easily into the slow-roll framework and allows inflation to continue for a longer number of e-foldings.

[34] Allowing for fourth or higher derivatives can increase the number of e-foldings, as is the case with large-field chaotic models with sinusoidal modulations (Kobayashi & Takahashi 2011) or extra-dimensional natural inflation models (Feng et al. 2003).

As we conclude this section on running, it is worth reiterating that the statistical preference for running is less than 3σ. However, the other model extensions we consider do not significantly weaken this preference for running. If the constraints from future experiments confirm this preferred value of running, it would represents an important clue about the earliest epochs of the universe.

8. CONSTRAINTS ON OTHER ONE-PARAMETER EXTENSIONS

In this section, we consider other physically motivated models that can affect the scale-dependence of the tilt of the CMB power spectrum. Specifically, we test the effect of (1) varying the effective number of neutrino species ($N_{\rm eff}$), a probe of the standard model of particle physics, and (2) an increase in the primordial fraction of baryonic mass in helium (Y_p), a possible signature of non-standard BBN. These extensions can increase the predicted damping due to photon diffusion relative to ΛCDM, which preferentially decreases small-scale power. The data therefore favor these extensions. Conversely, the data will disfavor extensions that exacerbate the discrepancy between the observed and predicted small-scale power. Examples of this type of extension include the tensor-scalar ratio r, which as discussed in S12 leads to larger values of n_s, and the effect of early dark energy, which we consider below.

8.1. $N_{\rm eff}$

In the standard thermal history, the radiation density in the early Universe is given by

$$\rho_r = \rho_\nu + \rho_\gamma = (1 + 0.227\, N_{\rm eff})\rho_\gamma, \qquad (11)$$

where ρ_γ is the photon density, a quantity measured extremely well by *COBE*/FIRAS (Fixsen et al. 1996), and $N_{\rm eff}$ is an effective number of neutrino species. The factor of 0.227 is calculated assuming all the entropy of e^+, e^- annihilation goes into the photons. This assumption is not perfect; the small correction due to the neutrinos gaining some entropy has traditionally been incorporated into $N_{\rm eff}$. For the standard model of three neutrino species, $N_{\rm eff} = 3.046$ (Dicus et al. 1982; Lopez et al. 1999; Mangano et al. 2005). Although generally discussed in the context of extra neutrino species, $N_{\rm eff}$ parametrizes the total non-photon contribution to the radiation density and thus includes contributions from any weakly/non-interacting, relativistic particles.

As described by Bashinsky & Seljak (2004) and Hou et al. (2013), the SPT+*WMAP* data constrain $N_{\rm eff}$ through its effects on the expansion rate at early times. Both the sound horizon r_s and the square of the damping length r_d depend on an integral with an integrand proportional to $1/H(z)$. However, the angular power spectrum is sensitive to the corresponding angular scales $\theta_d = r_d/D_A$ and $\theta_s = r_s/D_A$, where D_A is the angular-diameter distance to recombination. Since the angular-diameter distance is not known, measurements of θ_d or θ_s alone do not constrain the expansion rate well. The dependence on the unknown angular-diameter distance can be removed by looking at the ratio $r_d/r_s = \theta_d/\theta_s$. As the effect $N_{\rm eff}$ has on the expansion rate is roughly redshift independent, its effect can be pulled out of the integral, so in this extension $\theta_d/\theta_s \propto H^{1/2}$. A second effect of $N_{\rm eff}$ is on the phase of the acoustic oscillations. Constraints from this phase shift are subdominant in the ΛCDM+$N_{\rm eff}$ model, but become more important when Y_p is also allowed to vary; we discuss this effect in that context in § 9. The $N_{\rm eff}$ constraint in the ΛCDM+$N_{\rm eff}$ model can thus be interpreted through its effect on the θ_d/θ_s ratio.

Here we hold Y_p to the value predicted by BBN, which is a function of both $N_{\rm eff}$ and ω_b. These Y_p predictions are implemented in CosmoMC through interpolating over a table produced using PArthENoPE v1.00 (Pisanti et al. 2008). We look at the effect of varying Y_p independent of BBN constraints later in this section, and we consider jointly varying $N_{\rm eff}$ and Y_p independently in § 9.

The left panel of Figure 14 shows the CMB constraints on θ_d/θ_s in the ΛCDM+$N_{\rm eff}$ model space. The parameter θ_s is well-measured by both SPT and *WMAP*7, and the fractional shift in preferred θ_s is small between the two datasets. As a result, the uncertainty in $N_{\rm eff}$ is primarily due to the uncertainty in θ_d. In ΛCDM, θ_d is primarily constrained from the *WMAP*7 determinations of ω_b and ω_m – not by the damping tail measurement. Freeing $N_{\rm eff}$ greatly broadens the *WMAP*7 constraint on θ_d due to a degeneracy between $N_{\rm eff}$ and ω_m. With $N_{\rm eff}$ free, the SPT determination of θ_d from the damping tail becomes tighter than that from *WMAP*7.

Constraints on $N_{\rm eff}$ are shown in the right panel of Figure 14. The dot-dashed blue curve marks the broad *WMAP*7 posterior; Komatsu et al. (2011) find $N_{\rm eff} > 2.7$ (95% CL) using *WMAP*7 alone. As expected from the observed shift in θ_d/θ_s between *WMAP*7 and SPT, the SPT data prefer lower values of $N_{\rm eff}$ than *WMAP*7. Adding the SPT data to *WMAP*7 markedly improves the measurement as shown by the black curve. The joint SPT+*WMAP*7 constraint is:

$$N_{\rm eff} = 3.62 \pm 0.48,$$

representing a 20% reduction in uncertainty from the constraint determined from the *WMAP*7+K11 bandpowers. For the CMB data, the probability that $N_{\rm eff} > 3.046$ is 89%. In Table 4, we report the constraint on $N_{\rm eff}$ from the datasets discussed in this section, including constraints on other parameters of particular interest.

We now turn to the addition of the late-time BAO and H_0 data. When $z_{\rm eq}$ is held fixed at its well-measured value from the CMB, increasing the effective number of neutrino species results in an increased expansion rate, which decreases r_s. Since θ_s is well constrained, this results in a decrease in the angular-diameter distance D_A, and thus D_V. The end result is that, for the BAO observable r_s/D_V, the changes largely cancel. The CMB+BAO constraint is $N_{\rm eff} = 3.50 \pm 0.47$. The direct H_0 measurement is more sensitive to the value of $N_{\rm eff}$. However, the H_0 and CMB datasets prefer similar values of $H_0$and the preferred value of $N_{\rm eff}$ hardly moves when H_0 data is added. The resulting CMB+H_0 constraint is $N_{\rm eff} = 3.46 \pm 0.35$. The significance of the preference for $N_{\rm eff} > 3.046$ is largely unchanged between these three cases: the CMB, CMB+BAO, and CMB+H_0 prefer $N_{\rm eff} > 3.046$ at $1.2\,\sigma$, $1.0\,\sigma$, and $1.2\,\sigma$, respectively.

Though adding BAO or H_0 data individually to the CMB data slightly reduces the preferred value of $N_{\rm eff}$, combining all three datasets has the opposite effect of

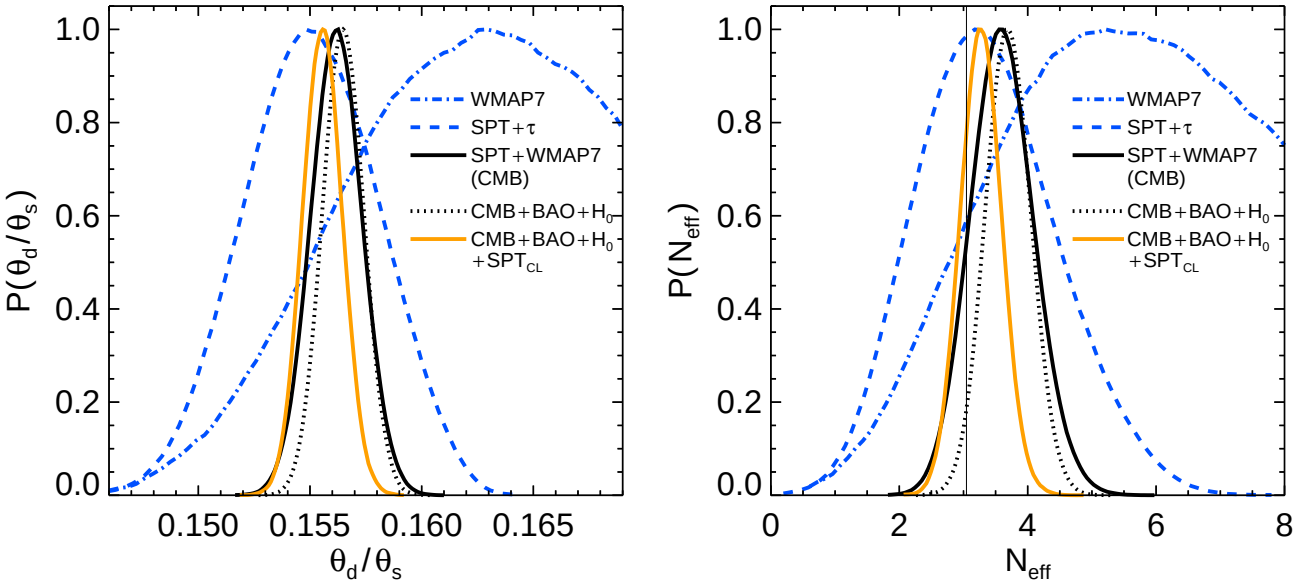

FIG. 14.— The marginalized one-dimensional posteriors for θ_d/θ_s (*left*) and $N_{\rm eff}$ (*right*) from various combinations of datasets. The constraint on $N_{\rm eff}$ in the ΛCDM+$N_{\rm eff}$ model for different combinations of datasets can be interpreted from the corresponding θ_d/θ_s posterior. The shift in θ_d/θ_s between broad *WMAP*7 (dot-dashed blue curve) and SPT (dashed blue curve) implies a preference for lower $N_{\rm eff}$ with SPT than *WMAP*7. The $N_{\rm eff}$ posterior of SPT+*WMAP*7 is shown by the solid black curve. The tighter constraints on $N_{\rm eff}$ can be obtained by adding BAO and H_0 (black dotted curve) and combining CMB, BAO, H_0 and SPT SZ-selected clusters (solid orange curve).

shifting the distribution towards slightly higher $N_{\rm eff}$. The joint CMB+BAO+H_0 constraint is $N_{\rm eff} = 3.71 \pm 0.35$, a $1.9\,\sigma$ preference for $N_{\rm eff} > 3.046$. The reasons for this shift can be seen in Figure 4. Increasing $N_{\rm eff}$ moves the CMB-predicted H_0 and BAO quantities towards the measured values. This ability of high $N_{\rm eff}$ to reconcile the CMB with BAO and H_0 has been noted previously by, e.g., Anderson et al. (2012). The inclusion of the BAO and H_0 information leads to a small upward shift in the value of $N_{\rm eff}$; a higher value of $N_{\rm eff}$ is required to reduce the tension between these datasets than that inferred from the CMB determination of θ_d/θ_s.

Prior to the decay of the gravitational potentials, the additional radiation density from extra neutrino species deepens potential wells, thus boosting structure growth at very early times. This increases the predicted abundance of massive galaxy clusters today. We therefore combine the $\rm SPT_{CL}$ galaxy cluster counts with CMB, BAO and H_0 data to obtain the tightest constraint on the number of effective neutrino species,

$$N_{\rm eff} = 3.29 \pm 0.31. \quad (12)$$

This is consistent at less than 1 sigma with the standard model of 3 neutrino species.

The effective number of neutrino species is partially degenerate with other extensions to ΛCDM, in particular, $dn_s/d\ln k$, Y_p, and $\sum m_\nu$. Including $dn_s/d\ln k$ shifts the preferred value of $N_{\rm eff}$ down by $1\,\sigma$ to $N_{\rm eff} = 2.98 \pm 0.38$; the effect of including Y_p is nearly identical. Including $\sum m_\nu$ has the opposite effect and moves the preferred value of $N_{\rm eff}$ up by $1\,\sigma$ to $N_{\rm eff} = 3.86 \pm 0.37$. The slight preference for $N_{\rm eff} > 3$ disappears when either $dn_s/d\ln k$ or Y_p are freed, but is strengthened when freeing $\sum m_\nu$.

In summary, CMB data primarily constrain $N_{\rm eff}$ through measurements of the ratio θ_d/θ_s. Adding H_0 and BAO measurements tightens this constraint and leads to a modest ($1.9\,\sigma$) preference for more than 3 neutrino species. This preference is driven by tension between the BAO and H_0 datasets. The tightest constraints come from the combination of the CMB, BAO, H_0 and cluster abundances and are consistent with 3 neutrino species at $0.8\,\sigma$. The $N_{\rm eff}$ constraints are sensitive to the addition of further model extensions.

8.2. Y_p

When the universe cools to $T \sim 0.1\,$MeV, light nuclei begin to form, a process known as big bang nucleosynthesis (BBN, Schramm & Turner 1998; Steigman 2007). The primordial fraction of baryonic mass in ^{4}He is denoted as Y_p. As mentioned in § 8.1, BBN makes a precise prediction for the primordial helium abundance. A useful analytic form is given by Simha & Steigman (2008), valid for $N_{\rm eff}$ near the standard model prediction:

$$Y_p = 0.2485 + 0.0016\,[(273.9\,\omega_b - 6) + 100(S-1)], \quad (13)$$

where

$$S^2 = 1 + (7/43)(N_{\rm eff} - 3.046). \quad (14)$$

The S^2 factor accounts for any non-standard expansion rate prior to and during BBN. We use the BBN prediction for Y_p in nearly all MCMCs, unless we specifically state that Y_p is free.

At fixed baryon density, increasing the helium fraction leads to increased damping. Helium has a higher binding energy and thus recombines earlier than hydrogen; each neutral helium atom effectively absorbs four free electrons at the surface of last scattering. This decreases the number of free electrons which increases the photon diffusion length, r_d, as seen in Equation 4. Mirroring § 8.1, this single distance measure is degenerate with the angular diameter distance to last scattering. However, since the sound horizon scale is nearly independent of Y_p, the

TABLE 4
ΛCDM+ $N_{\rm eff}$ Results from SPT, CMB, CMB+BAO, CMB+H_0 and CMB+BAO+H_0

[a]As calculated from BBN theory

Datasets	$N_{\rm eff}$	Y_p [a]	$10^2\Omega_b h^2$	H_0 [km s^{-1} Mpc^{-1}]	$z_{\rm eq}$	$10\,\theta_d/\theta_s$
SPT+τ	$3.36^{+1.16}_{-1.03}$	0.252 ± 0.014	2.307 ± 0.122	$77.1^{+9.0}_{-8.1}$	3053 ± 192	1.552 ± 0.030
CMB	3.62 ± 0.48	0.255 ± 0.006	2.268 ± 0.049	75.9 ± 3.4	3136 ± 96	1.562 ± 0.011
CMB+BAO	3.50 ± 0.47	0.254 ± 0.006	2.232 ± 0.045	71.4 ± 2.5	3326 ± 50	1.561 ± 0.011
CMB+H_0	3.46 ± 0.35	0.253 ± 0.005	2.253 ± 0.038	74.5 ± 1.9	3161 ± 84	1.559 ± 0.009
CMB+BAO+H_0	3.71 ± 0.35	0.256 ± 0.004	2.247 ± 0.038	72.6 ± 1.8	3322 ± 49	1.565 ± 0.009
CMB+BAO+H_0+SPT$_{\rm CL}$	3.29 ± 0.31	0.251 ± 0.004	2.223 ± 0.037	71.2 ± 1.7	3268 ± 43	1.556 ± 0.009

This table shows constraints on the ΛCDM+ $N_{\rm eff}$ model. In addition to $N_{\rm eff}$, we include constraints on other parameters of particular interest for this extension. In this model space, Y_p is related to $\Omega_b h^2$ and $N_{\rm eff}$ by a BBN consistency relation.

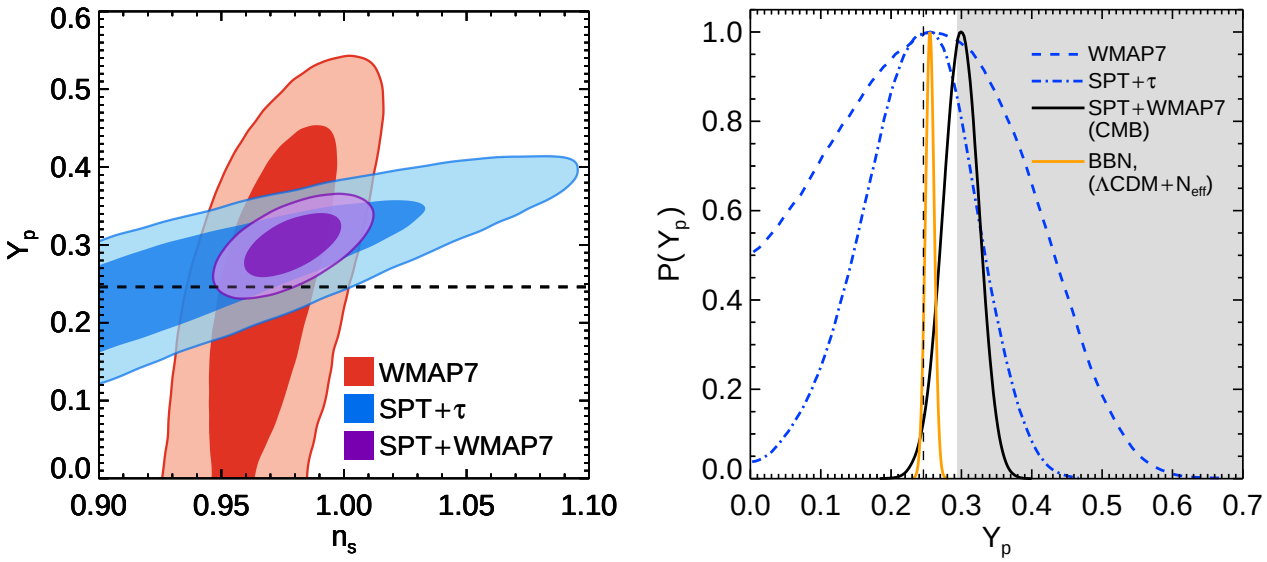

FIG. 15.— The CMB data place independent constraints on the primordial helium abundance, Y_p. ***Left panel:*** The contours show the two-dimensional 68% and 95% confidence intervals for Y_p and n_s for three datasets: SPT, *WMAP*7, and SPT+*WMAP*7. The BBN prediction for 3 neutrino species is marked by the horizontal black dashed line at $Y_p = 0.2478$. The change in the damping scale due to varying Y_p can be mimicked by changing n_s for the SPT data. *WMAP*7 provides an independent measurement of n_s, greatly enhancing the SPT+*WMAP*7 measurement of the helium abundance. ***Right panel:*** The marginalized one-dimensional posteriors for Y_p in different model and data combinations. We show constraints from the SPT (blue dot-dashed line), *WMAP*7 (blue dashed line), and SPT+*WMAP*7 (black solid line). The BBN prediction for 3 neutrino species is marked by the vertical black dashed line at $Y_p = 0.2478$. The orange solid line shows the marginally wider BBN prediction from the ΛCDM+$N_{\rm eff}$ MCMC chain. The grey area is ruled out by the 95% upper limit from the protosolar helium abundance. The preference of the CMB for higher helium abundances can be reduced by introducing other extensions that affect small scale power, as is demonstrated in § 9.1.

ratio of θ_d/θ_s breaks the degeneracy with D_A and allows the CMB data to constrain Y_p independently of BBN.

Precise experimental inferences of Y_p have come from spectral observations of extragalactic clouds of low-metallicity ionized gas (Izotov et al. 2007; Peimbert et al. 2007; Izotov & Thuan 2010; Aver et al. 2010, 2011, 2012). Historically, these results have shown substantial variations between groups that greatly exceed the expected statistical variations; for a more complete discussion of these measurements, see e.g., Aver et al. (2010). Marginalizing over all possible trends of the estimated Y_p with metallicity increases the uncertainty substantially: for example, Aver et al. (2012) find $Y_p = 0.2534 \pm 0.0083$, $0.7\,\sigma$ above the BBN prediction for Y_p assuming the three standard neutrino species and the value of ω_b measured by *WMAP*.

An upper limit to Y_p can be inferred from protosolar abundance estimates resulting from helioseismology; Serenelli & Basu (2010) find the protosolar helium abundance to be $Y_{\rm solar} = 0.278 \pm 0.008$. This measurement relies upon well-studied gravitational and solar evolution physics to back out the protosolar abundance from current measurements of the helium fraction on the solar surface. It is difficult to imagine mechanisms by which the protosolar abundance is reduced below the primordial helium abundance. Therefore some measure of caution is warranted in interpreting cosmological constraints with primordial helium abundances above the $2\,\sigma$ upper limit of $Y_p < 0.294$ derived from these measurements.

After combining *WMAP*7 with ACBAR and QUaD temperature power spectra, Komatsu et al. (2011) determine $Y_p = 0.326 \pm 0.075$. Dunkley et al. (2011) obtain $Y_p = 0.313 \pm 0.044$ by combining the ACT and WMAP7

data. Using the bandpowers from the first 790 deg^2 SPT survey and WMAP7 data, K11 find $Y_p = 0.296 \pm 0.030$. In this analysis, we infer $Y_p = 0.240 \pm 0.079$ with the SPT bandpowers alone. These results are shown in the right panel of Figure 15. The combined CMB data lead to:

$$Y_p = 0.300 \pm 0.025. \quad (15)$$

As shown in the left panel of Figure 15, the addition of the *WMAP* 7 data breaks a degeneracy present in the SPT data between Y_p and n_s. The fact that the resulting Y_p is higher than the BBN-consistent value reflects the fact that, in the ΛCDM model, where Y_p is required to be BBN-consistent, SPT prefers a lower value of n_s than does *WMAP*7. Since Y_p has none of the late-time effects of neutrino species, adding BAO and H_0 data hardly change the Y_p constraint. The constraint from CMB+BAO+H_0 is $Y_p = 0.305 \pm 0.024$. However, slightly more than half the parameter space allowed by the CMB+BAO+H_0 data is ruled out by the protosolar upper limit.

The constraints presented above can also be compared to the BBN predicted value of $Y_p = 0.24774 \pm 0.00014$. The $\sim$0.06% uncertainty quoted here does not include the 0.2% theoretical uncertainty on Y_p in the PArthENoPE code used in CAMB (Pisanti et al. 2008). The inferred Y_p value for CMB+BAO+H_0 is $2.4\,\sigma$ above the BBN prediction. We explore the relationship between the damping-tail inference of Y_p and the BBN prediction in more detail in § 9, where we consider an expanded model with both Y_p and $N_{\rm eff}$ free. It is worth repeating that the feature of the CMB data that drives these high values of Y_p – a trend of decreasing power at higher multipoles relative to ΛCDM predictions – can also be explained by other model extensions, such as $dn_s/d\ln k$ or $N_{\rm eff}$, both discussed above.

8.3. *Early dark energy*

The dark energy density could be considerable in the early universe if the equation of state parameter w was much larger in the past, a situation commonly referred to as early dark energy. Early dark energy models lead to much larger signatures in the CMB anisotropy than traditional dark energy models; see Reichardt et al. (2012) for a discussion of the effects of early dark energy. One reason these models are interesting is that they can be constructed with attractor solutions that reduce the necessity to fine-tune the initial conditions (Wetterich 1988; Ratra & Peebles 1988). For instance in "tracer" models, the dark energy equation of state is required to be equal to the background equation of state – e.g., during radiation domination, $w = 1/3$. The advantages are that the DE density can stay much closer to the energy density of the dominant component and that the DE evolution is independent of initial conditions.

Instead of considering a specific model, we choose to constrain early dark energy in the more general tracer model parametrization by Doran & Robbers (2006). This parametrization introduces two new parameters in addition to the ΛCDM set, the dark energy equation of state at $z = 0$, w_0, and the dark energy density relative to the critical density at early times, $\Omega_{\rm e}$, which is taken to be constant at sufficiently high redshift ($z \gtrsim 10$). The dark energy density and equation of state are then given by

$$\Omega_{\rm de}(a) = \frac{\Omega^0_{\rm de} - \Omega_{\rm e}\left(1 - a^{-3w_0}\right)}{\Omega^0_{\rm de} + \Omega^0_{\rm m} a^{3w_0}} + \Omega_{\rm e}\left(1 - a^{-3w_0}\right) \quad (16)$$

$$w(a) = -\frac{1}{3[1 - \Omega_{\rm de}(a)]}\frac{d\ln\Omega_{\rm de}(a)}{d\ln a} + \frac{a_{eq}}{3(a + a_{eq})} \quad (17)$$

Here a_{eq} is the scale factor at matter-radiation equality, and $\Omega^0_{\rm de}$ ($\Omega^0_{\rm m}$) is the dark energy (matter) density relative to critical density at $z = 0$. The dark energy equation of state today is w_0. This parametrization assumes spatial flatness so that $\Omega^0_{\rm m} + \Omega^0_{\rm de} = 1$. Since we force $\Omega_{\rm de}(a)$ to be constant at high redshift, the dark energy equation of state mimics that of the dominant component at early times, thus behaving like a tracer model. Later, during matter domination at $z < 10$, the equation of state transitions towards its current value, w_0, so it can account for cosmic acceleration.

To consistently describe the perturbations, we are motivated by quintessence models to treat dark energy as a perfect fluid with a sound speed, c_s, equal to the speed of light (see Hu 1998). This choice, together with the parametrization for the background evolution, completely specifies the behavior of dark energy. We require $w_0 \geq -1$ and thus do not entertain the possibility of "phantom crossing" (see, e.g., Fang et al. 2008). This restriction allows us to avoid pathologies in perturbation evolution and to stay in the quintessence regime.

Like all the other extensions, early dark energy changes the tilt of the CMB power spectrum between small and large scales. The addition of SPT data therefore helps to further constrain the level of early dark energy. For a detailed physical explanation of how early dark energy is constrained by the CMB data, see Reichardt et al. (2012).

The small-scale CMB temperature anisotropy power measurement from the SPT bandpowers improves the constraints on the early dark energy density over WMAP7 alone by a factor of 3.5; the 95% upper limit on $\Omega_{\rm e}$ is reduced from 0.052 for WMAP7-only to 0.013 for WMAP7+SPT. This is a 38% improvement on the upper limit of $\Omega_{\rm e} < 0.018$ reported for WMAP7+K11 (Reichardt et al. 2012). Adding low-redshift geometrical measurements does not help constrain early dark energy, although, these data have a dramatic effect on the quality of the constraints on the late-time dark energy density and equation of state. The upper limit is essentially unchanged at $\Omega_{\rm e} < 0.014$ for WMAP7+SPT+BAO+SNe. The $\Omega_{\rm e} < 0.013$ bound from WMAP+SPT is the best published constraint from the Cosmic Microwave Background.

9. TWO-PARAMETER EXTENSIONS

We will now consider two 2-parameter extensions to ΛCDM: $N_{\rm eff}$+Y_p and $N_{\rm eff}$+$\sum m_\nu$. Of the many possible 2-parameter combinations, we limit our discussion to these two extensions because they are physically well-motivated. The first case is an interesting consistency test of BBN, while the second case is a natural space to consider for sterile neutrinos.

9.1. $N_{\rm eff}$ *and* Y_p

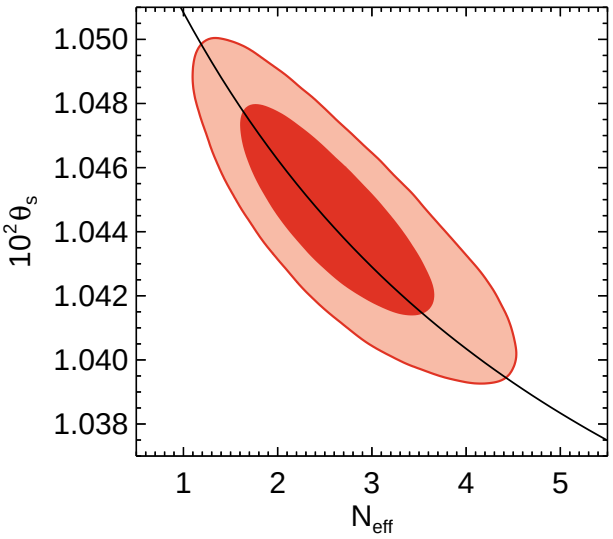

FIG. 16.— Changing $N_{\rm eff}$ introduces phase shifts in the acoustic oscillations, however, constraints on these phase shifts are weakened by a degeneracy between $N_{\rm eff}$ and θ_s. Here, we show the marginalized two-dimensional posteriors for $N_{\rm eff}$ and θ_s from the CMB data for the ΛCDM+$N_{\rm eff}$+Y_p model. The black curve shows the correlation between the two parameters due to the phase shifts in the acoustic oscillations. This curve is defined using the Bashinsky & Seljak (2004) prescription for the phase shifts, normalized to the best-fit $\theta_s = 1.0429 \times 10^{-2}$ at $N_{\rm eff} = 3.046$.

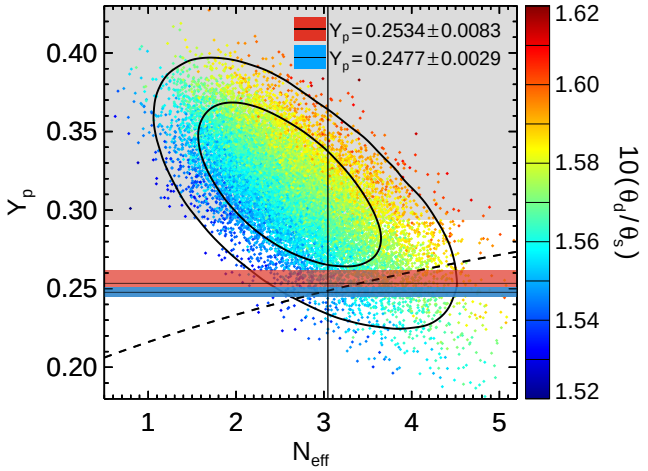

FIG. 17.— This plot contrasts the CMB-derived two-dimensional likelihood contours for $N_{\rm eff}$ and Y_p with the predictions of BBN and other Y_p measurements. The black solid contours are the 68% and 95% confidence intervals for SPT+*WMAP*7. The scattered points are samples from the Markov chain with the color encoding the value of θ_d/θ_s. The dashed black curve marks the standard BBN relationship between $N_{\rm eff}$ and Y_p. Similar to the right panel of Figure 15, the gray area is ruled out by the 95% upper limit of the measurement of solar initial helium abundance by Serenelli & Basu (2010). The Y_p measurement from spectral observations of extragalactic low-metallicity ionized gas clouds by Peimbert et al. (2007) and Aver et al. (2012) are shown by the light blue and red bands respectively.

Here we examine simultaneous constraints on the effective number of neutrino species and the primordial abundance of ^{4}He: ΛCDM+$N_{\rm eff}$+Y_p. This two-parameter extension to ΛCDM is moderately favored by the data with a $\Delta\chi^2 = 5.5$ (see Table 2), though it does little to ease the tension between datasets beyond the one-parameter ΛCDM+$N_{\rm eff}$ model.

We first discuss the physical mechanisms that lead to joint constraints on $N_{\rm eff}$ and Y_p. As noted earlier in § 8.1 and 8.2, both the number of neutrinos and helium abundance primarily impact the damping scale. However, the parameters are not fully degenerate due to several additional effects of varying $N_{\rm eff}$ as discussed in Hou et al. (2013). Here we highlight in particular the role of shifts in the acoustic peak locations induced by phase shifts in the acoustic oscillations (Bashinsky & Seljak 2004).

Acoustic oscillations in a constant gravitational potential will have the form $\cos(kr_s(\eta) + \varphi)$, where k is the wavenumber and the phase $\varphi = 0$ as a consequence of the initial conditions in inflation models. Changes in the gravitational potentials shift the phase away from zero. Unlike photons, neutrinos have a long free-streaming distance in the early plasma. They thus alter the evolution of the gravitational potential and therefore the resulting phase shifts. For modes that entered the horizon in the radiation-dominated era ($l > l_{eq} \simeq 434$), Bashinsky & Seljak (2004) find that the change to the phase shift due to neutrino free streaming is $\Delta\varphi = 0.19\pi\rho_\nu/(\rho_\nu + \rho_\gamma)$. Here ρ_γ and ρ_ν are the energy densities of the photons and neutrinos respectively. This phase shift changes the positions of the acoustic peaks in the CMB data.

Constraints on the phase shifts are weakened by a partial degeneracy between the angular size of the sound horizon and a phase shift. This point is illustrated by Figure 16 which shows the 68% and 95% confidence intervals on $N_{\rm eff}$ and θ_s from the CMB. Changing the phase shift by $\delta\varphi$ and the sound horizon by $\delta\theta_s$ moves the $m^{\rm th}$ acoustic peak by $\delta l_m = (\delta\varphi - l_m\delta\theta_s)/\theta_s$. We can thus hold fixed the position of any single acoustic peak by varying θ_s to accommodate the phase shift. The black curve in the figure is the locus of points that does exactly this, although not for a particular peak but for a particular l value. We chose $l = 1666$ because it is approximately where the signal-to-noise is maximized in the SPT bandpowers. The major axis of the constraint ellipse falls along the black line, confirming that the calculated phase shifts explain the observed correlation between $N_{\rm eff}$ and θ_s. The degeneracy between $N_{\rm eff}$ and θ_s is broken (the contours close) in part because the compensating value of θ_s is l-dependent; there is no one value of θ_s that preserves all the peak locations. Other effects play a role in the degeneracy breaking as well, including the early ISW effect and effects due to the high values of the baryon fraction that occur at low $N_{\rm eff}$ (Hou et al. 2013).

The $N_{\rm eff}$-Y_p contours from the CMB dataset are shown in Figure 17. The contours form an ellipse, with the minor axis (the better constrained direction) oriented in the direction of varying θ_d/θ_s. Relative to *WMAP*7+K11, the new SPT bandpowers have the most impact on the high $N_{\rm eff}$ region. This improved constraint on $N_{\rm eff}$ is due to improved constraints on the neutrino-induced phase shifts.

The inferred values of $N_{\rm eff}$ and Y_p for the CMB data are:

$$Y_p = 0.314 \pm 0.033, \qquad (18)$$
$$N_{\rm eff} = 2.60 \pm 0.67.$$

When the BAO and H_0 observations are added, the median values of these parameters shift slightly towards

the standard model expectations, and the uncertainties tighten:

$$Y_p = 0.294 \pm 0.030, \quad (19)$$
$$N_{\rm eff} = 3.32 \pm 0.45.$$

We compare these CMB-derived results with the predictions from BBN theory (see Equation 13) in Figure 17. The dashed curve in Figure 17 denotes the BBN theory predictions. The data are consistent with BBN theory, although they display a mild preference for higher-than-predicted values of Y_p. The region above the $2\,\sigma$ upper limit from the initial solar helium abundance (Serenelli & Basu 2010) is greyed out. We also plot the Peimbert et al. (2007) and Aver et al. (2012) estimates of Y_p based on spectroscopic observations of low-metallicity extragalactic clouds (see § 8.2) as horizontal bands. The CMB+BAO+H_0 inference for the helium abundance is consistent with the spectroscopic observations of Aver et al. (2012) at $1.3\,\sigma$.

In summary, the CMB data can constrain Y_p and $N_{\rm eff}$ simultaneously by measuring the damping scale and the location of the acoustic peaks. The combination of CMB+BAO+H_0 prefers a value of $N_{\rm eff}$ which is consistent with three neutrinos species and a value of Y_p slightly above the BBN prediction.

9.2. $N_{\rm eff}$ *and* $\sum m_\nu$

We finally focus on a two-parameter extension, ΛCDM+$\sum m_\nu$+$N_{\rm eff}$, in which both the mass and number of neutrino species are freed. This is a well-motivated, natural model expansion of the individual $\sum m_\nu$ and $N_{\rm eff}$ extensions discussed earlier since (1) neutrino oscillation experiments have established that neutrinos are massive (Hamish Robertson 2009) and (2) the event excess in the MiniBooNE search for $\bar{\nu}_\mu \to \bar{\nu}_e$ oscillations (Aguilar-Arevalo et al. 2010) and the reactor antineutrino anomalies (Mention et al. 2011) suggest one or more massive ($\sim 1\,$eV) sterile neutrino species. We will continue to assume equal masses in all neutrino species. For treatments of (3+1) or (3+2) models in the literature, see e.g. Kopp et al. (2011) or Giunti & Laveder (2011).

Cosmological observations can rule out large areas of the $N_{\rm eff}$-$\sum m_\nu$ plane. Benson et al. (2013) investigated constraints from *WMAP*7, K11, BAO, H_0, and SPT galaxy clusters, and found $N_{\rm eff} = 3.91 \pm 0.42$ and $\sum m_\nu = (0.34 \pm 0.17)\,$eV. A more recent study by Riemer-Sørensen et al. (2013) used WMAP7+K11+WiggleZ+$H(z)$+SNLS3 to measure $N_{\rm eff} = 3.58^{+0.15}_{-0.16}$ (68% CL) and $\sum m_\nu < 0.60\,$eV (95% CL). The tightness of the constraints on $N_{\rm eff}$ from this study are driven by the inclusion of the $H(z)$ inference from measuring the age-redshift relation of passively evolving galaxies out to $z \sim 1.75$ (Moresco et al. 2012), which depends heavily on modeling stellar evolution. The extended arm out to higher redshifts provides greater constraining power on the expansion history, placing constraints on $N_{\rm eff}$; conversely, this information has little impact on the neutrino mass constraint.

As discussed in § 4.2, this two-parameter extension significantly improves the quality of fit to the CMB+BAO+H_0 data by $\chi^2 = 7.9$, equivalent to a $2.3\,\sigma$ Gaussian preference. This model also increases the consistency between the CMB, BAO, and H_0 datasets, as illustrated by Figure 18. Both panels show the $r_s/D_V(z = 0.57)$–H_0 plane and are identical except for the color-coding, which encodes $N_{\rm eff}$ in the left panel and $\sum m_\nu$ in the right panel. Like the ΛCDM+$N_{\rm eff}$ model shown in Figure 4, this 2-parameters extension allows the contours from the three datasets to overlap comfortably.

$N_{\rm eff}$ and $\sum m_\nu$ are individually constrained by separate features in the CMB as described in § 6 and § 8.1 – the early ISW effect for $\sum m_\nu$, the damping scale and the position of the acoustic peaks for $N_{\rm eff}$. We can use Figure 18 to understand phenomenologically the relative interplay between $N_{\rm eff}$, $\sum m_\nu$, H_0, and the BAO features, given a CMB prior. In the left panel, $N_{\rm eff}$ increases as H_0 increases and r_s/D_V decreases. The detailed direction means that the H_0 measurement is much more constraining than BAO for $N_{\rm eff}$, similar to the constraint on individual $N_{\rm eff}$ discussed in § 8.1. In the right panel, the BAO data are critical for the neutrino mass measurement, whereas varying H_0 at fixed r_s/D_V (horizontal lines in the figure) has almost no effect on $\sum m_\nu$. This can also be seen by the significant tightening of the inferred mass uncertainty between the green and blue contours in Figure 19. We see in Figure 19 that there is a positive correlation between $N_{\rm eff}$ and $\sum m_\nu$ when H_0 is one of the datasets. This correlation emerges because the only way to increase $N_{\rm eff}$ in this model space while fixing $z_{\rm eq}$, θ_s and H_0 is to increase $\sum m_\nu$ (and decrease Ω_Λ).

The CMB constraints on $N_{\rm eff}$ and $\sum m_\nu$ are nearly independent as shown by the red contours of Figure 19. As would be expected for independent parameters, the quality of the constraints are nearly unchanged from the single-parameter extensions discussed earlier. The $N_{\rm eff}$ constraint is $N_{\rm eff} = 3.40 \pm 0.48$ with massive neutrinos compared to $N_{\rm eff} = 3.62 \pm 0.48$ in the earlier massless case. In both the ΛCDM+$\sum m_\nu$ and ΛCDM+$N_{\rm eff}$+$\sum m_\nu$ models, the CMB sets an upper limit on the neutrino masses of $\sum m_\nu < 1.6\,$eV (95% CL). This independence is broken, and the constraints significantly tightened, once low-redshift observations are added. The green contours show the results of including H_0, while the blue contours show the constraints from CMB+BAO+H_0. For the combination of CMB+BAO+H_0 we find:

$$\sum m_\nu = (0.48 \pm 0.21)\,{\rm eV}, \quad (20)$$
$$N_{\rm eff} = 3.89 \pm 0.37.$$

As should be expected from § 6, the mass constraint can be improved by adding a tracer of structure growth. For CMB+BAO+H_0+SPT$_{\rm CL}$ (the purple contours, we find the tightest constraint of

$$\sum m_\nu = (0.51 \pm 0.15)\,{\rm eV}, \quad (21)$$
$$N_{\rm eff} = 3.86 \pm 0.37.$$

This is a greater than $3\,\sigma$ preference for $\sum m_\nu > 0$ and a $2.2\,\sigma$ preference for $N_{\rm eff} > 3.046$.

10. CONCLUSIONS

The SPT bandpowers as presented in Story et al. (2013) are currently the best measurements of the CMB damping tail from the third to ninth acoustic peaks

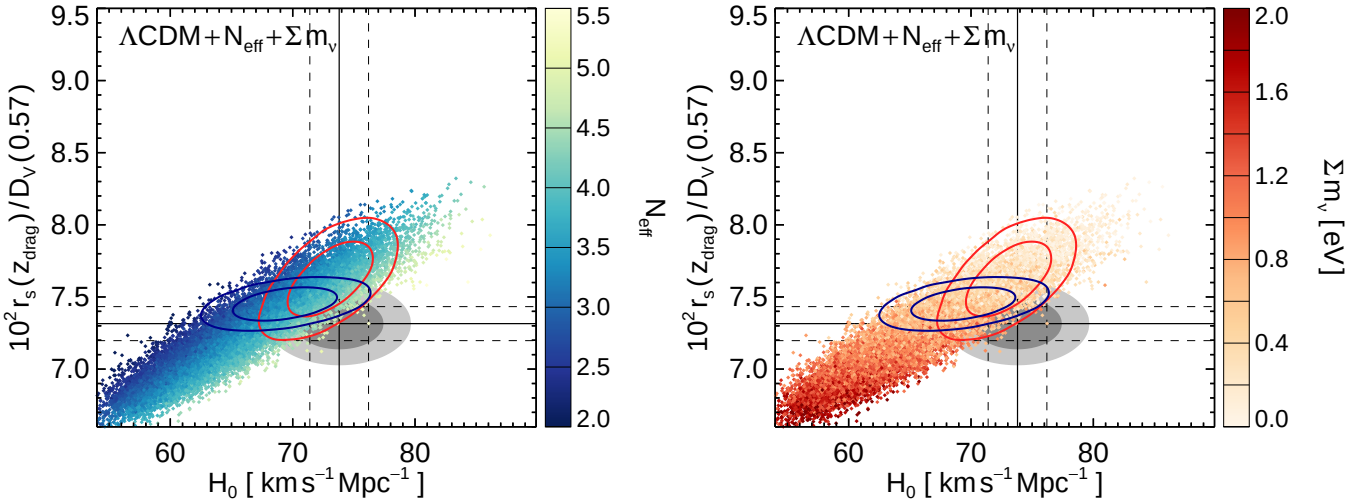

FIG. 18.— The $H_0 - r_s/D_V$ plane for the two-parameter extension ΛCDM+$N_{\rm eff}$+$\sum m_\nu$ with the color of scattered points coding the values of $N_{\rm eff}$ (left panel) and $\sum m_\nu$ (right panel). The colored contours and the gray filled regions are as described in Figure 4.

TABLE 5
HINTS FOR EXTENSIONS TO ΛCDM

Model extension	Preferred by the CMB data (see 1st row of Table 2)	Alleviates tension when combining BAO and H_0 data	Statistical error on extension parameter reduced by combining BAO and H_0 data
$\sum m_\nu$	*Marginal* $\Delta\chi^2 = 2.4$, 1 dof Figure 10	**No** Figure 4	**Yes** $\sigma_{\rm CMB+BAO+H_0}/\sigma_{\rm CMB} = 0.37$ Figure 10
$dn_s/d\ln k$	**Yes** $\Delta\chi^2 = 4.9$, 1 dof Figures 12 and 13	**No** Figure 4	**No** $\sigma_{\rm CMB+BAO+H_0}/\sigma_{\rm CMB} = 0.91$ Figure 12
$N_{\rm eff}$	**No** $\Delta\chi^2 = 1.1$, 1 dof Figure 14	**Yes** Figure 4	*Marginal* $\sigma_{\rm CMB+BAO+H_0}/\sigma_{\rm CMB} = 0.73$ Figure 14
$N_{\rm eff}$+$\sum m_\nu$	**No** $\Delta\chi^2 = 2.6$, 2 dof Figure 19	**Yes** Figure 18	**Yes** $\sigma_{\rm CMB+BAO+H_0}/\sigma_{\rm CMB} = 0.43$ $(\sum m_\nu)$ $\sigma_{\rm CMB+BAO+H_0}/\sigma_{\rm CMB} = 0.77$ $(N_{\rm eff})$ Figure 19

This table summarizes the evidence for physics beyond the ΛCDM model. We state our conclusions and relevant figures for each entry. The second column addresses whether the CMB alone shows a preference for the extension. The third column addresses whether the extension reduces the tension between the datasets. The $\Delta\chi^2$s in Table 2 quantify the preference and reduction in the tension. The final column shows if the extension is favored because the statistical errors are significantly reduced by adding datasets.

($650 \lesssim l \lesssim 3000$). The SPT bandpowers greatly improve measurements of three CMB observables: the damping scale due to photon diffusion, the locations of the acoustic peaks, and the amplitude of the lensing potential. The combined CMB data show a slight, reddening, scale-dependent tilt unreproducible in the ΛCDM model. Therefore, we find that while the SPT bandpowers are well-fit by a ΛCDM cosmology, there are tantalizing hints for extensions to this model.

With the aid of Table 5, we now summarize our most intriguing findings. The extension that the CMB data most prefer (at 2.4 σ) is the running of the spectral index, $dn_s/d\ln k$. This extension improves the fit to the CMB data, reducing the minimum χ^2 by $\Delta\chi^2 = 4.9$ from that achieved with ΛCDM. We find, for the CMB alone, $dn_s/d\ln k = -0.024 \pm 0.011$. Negative running of the spectral index reconciles the slightly redder spectral index preferred by the SPT data with the slightly bluer tilt preferred by the *WMAP*7 data; the same value of running is preferred by the *WMAP*7 data alone, although only at $\sim 1\,\sigma$. The combination of CMB, BAO, and H_0 data prefers more negative running, $dn_s/d\ln k = -0.028 \pm 0.010$. Deviations from scale invariance of this magnitude are not expected in standard inflationary scenarios.

Increasing the primordial helium abundance increases the damping scale which has a similar impact as negative running on the CMB power spectrum. Freeing the helium abundance reduces the minimum χ^2 of the combined CMB fit by $\Delta\chi^2 = 4.4$, resulting in $Y_p = 0.300 \pm 0.025$. However, this value of Y_p exceeds the protosolar 95% confidence upper limit of $Y_p < 0.294$. A summary of which extensions the CMB prefer can be found in Table 5.

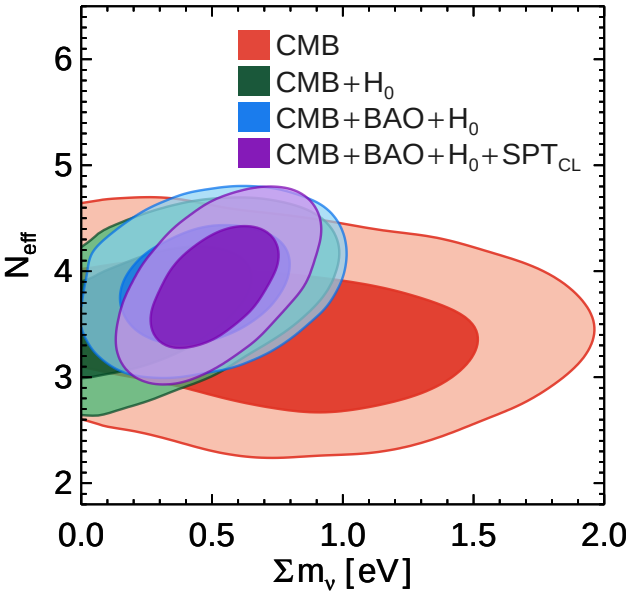

FIG. 19.— This figure demonstrates the impact of each combination of datasets on the constraints on $\sum m_\nu$ and $N_{\rm eff}$. The shaded contours are the 68% and 95% confidence intervals for the following data combinations: SPT+*WMAP*7 (CMB; red), CMB+H_0 (green), CMB+H_0+BAO (blue), CMB+H_0+BAO+SPT$_{\rm CL}$ (purple). The combined data are in $>2\,\sigma$ tension with the ΛCDM assumption of three massless neutrino species.

We also find that some extensions are more motivated than others with respect to how they reduce the mild tension between the CMB, H_0, and BAO datasets in the context of the ΛCDM model. The ability of various extensions to reduce this tension is shown in the third column of Table 5. Of the extensions that we consider, the effective number of neutrino species, $N_{\rm eff}$, is the only model extension that significantly reduces the tension between the CMB, BAO, and H_0 datasets. It does so both on its own, and when $\sum m_\nu$ is simultaneously free. The tension is reduced because $N_{\rm eff}$ brings the model predictions for CMB and H_0 into better agreement with data without much change in the prediction for the BAO observable r_s/D_V. Thus, this extension can bring the region of the CMB probability posterior that is more consistent with the measured r_s/D_V toward simultaneous compatibility with the H_0 measurement. Combining the CMB with BAO and H_0 data, we find $N_{\rm eff} = 3.71 \pm 0.35$. Simultaneously freeing $\sum m_\nu$ leads to further improvement in the fit as higher neutrino masses bring the CMB into better consistency with r_s/D_V, while increasing $N_{\rm eff}$ leads to consistency with H_0.

The impact of combining low redshift measurements with CMB data is summarized for selected extensions in the last column of Table 5. We find that the CMB, CMB+BAO, and CMB+SPT$_{\rm CL}$ all at least weakly prefer a non-zero neutrino mass (with only H_0 preferring zero mass). The combined CMB+BAO+H_0+SPT$_{\rm CL}$ dataset constrains $\sum m_\nu = (0.31 \pm 0.11)$ eV. The preference for massive neutrinos remains at $> 2\,\sigma$ as long as we keep at least one of the two most precise BAO measurements; however, it disappears if we do not include any BAO data.

We find improved constraints on two additional model extensions, early dark energy and non-zero curvature. These extensions do not address the scale-dependent tilt present in the data or lead to a reduction of the tension between the CMB and low-redshift data.

In summary, we explore six theoretically motivated extensions to the ΛCDM model, and find that the combination of the SPT data with other cosmological measurements yields a 2-3 σ preference for some of these extensions. Favored extensions are running of the primordial spectral index, a sum of neutrino masses of order 0.3 eV, or greater than 3 effective neutrino species. The evidence for any extension to the standard ΛCDM model is currently weak given we find a maximum preference of $3.0\,\sigma$ after considering a number of extensions and data sets. However, a significant detection of any of these extensions in future data sets such as *Planck* and high-resolution CMB polarization experiments would dramatically impact our understanding of particle physics and cosmology.

The SPT is supported by the National Science Foundation through grant ANT-0638937, with partial support provided by NSF grant PHY-1125897, the Kavli Foundation, and the Gordon and Betty Moore Foundation. The McGill group acknowledges funding from the National Sciences and Engineering Research Council of Canada, Canada Research Chairs program, and the Canadian Institute for Advanced Research. R. Keisler acknowledges support from NASA Hubble Fellowship grant HF-51275.01, B.A. Benson a KICP Fellowship, M. Dobbs an Alfred P. Sloan Research Fellowship, O. Zahn a BCCP fellowship. This research used resources of the National Energy Research Scientific Computing Center (NERSC), which is supported by the Office of Science of the U.S. Department of Energy under Contract No. DE-AC02-05CH11231, and the resources of the University of Chicago Computing Cooperative (UC3), supported in part by the Open Science Grid, NSF grant NSF PHY 1148698. We acknowledge the use of the Legacy Archive for Microwave Background Data Analysis (LAMBDA). Support for LAMBDA is provided by the NASA Office of Space Science.

APPENDIX

IMPACT OF EXTRAGALACTIC FOREGROUNDS AND OTHER SYSTEMATIC EFFECTS

One of the central findings of this paper is the preference in the data for lower power at small scales than would be predicted by the ΛCDM model conditioned on the *WMAP*7 data. In this appendix, we test the robustness of this preference to the priors on the beam, calibration and extragalactic foregrounds. For simplicity, we only consider two typical extensions: running of the spectral index and changes to Silk damping (parameterized by the helium abundance Y_p). We test how the marginalized constraints on $dn_s/d\ln k$ and Y_p change when the following systematic tests are performed:

- Doubling the width of foreground priors,

TABLE 6
THE MARGINALIZED CONSTRAINTS ON $dn_s/d\ln k$ AND Y_p FOR DIFFERENT SYSTEMATIC EFFECTS

Parameters	baseline	2× fg. prior width	no fg. prior	2× calib. uncert.	2× beam uncert.
$dn_s/d\ln k$	-0.024 ± 0.011	-0.026 ± 0.012	-0.029 ± 0.012	-0.025 ± 0.011	-0.033 ± 0.014
Y_p	0.300 ± 0.025	0.306 ± 0.027	0.323 ± 0.028	0.300 ± 0.025	0.311 ± 0.032

fg. - foreground
calib. - calibration
uncert. - uncertainty

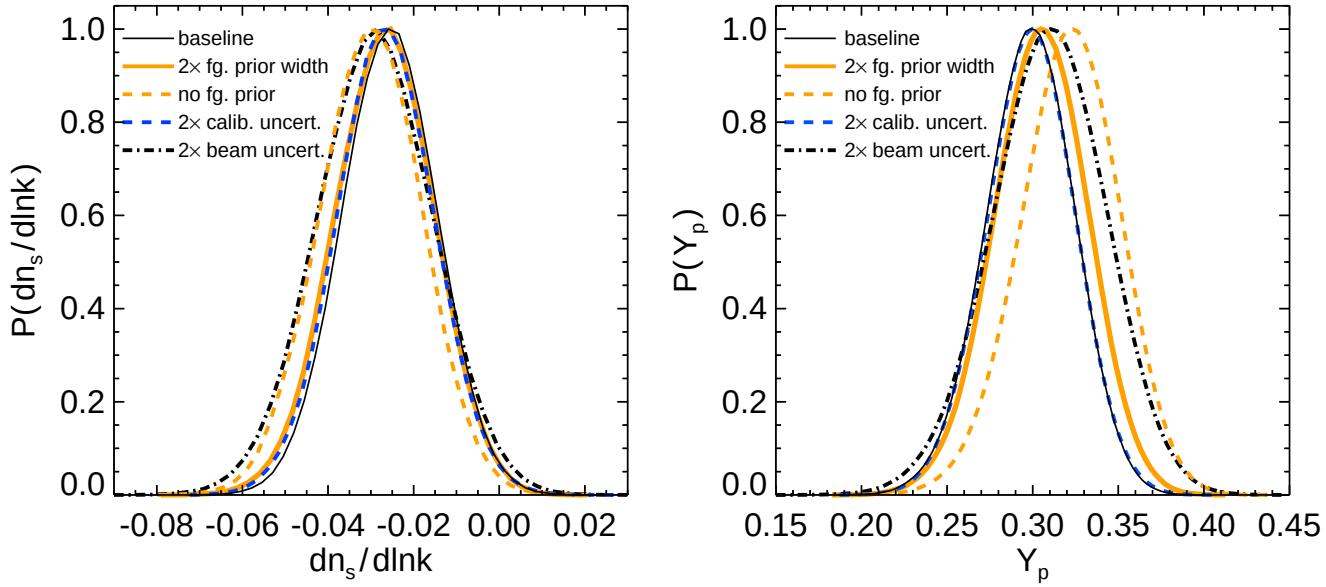

FIG. 20.— The preference for negative running or more damping (in terms of higher Y_p) are robust to the extra Galactic foreground modeling and other systematic effects. In both panel, 'fg.' refers to foreground, 'calib.' refers to calibration and 'uncert.' refers to uncertainty.

- Removing the foreground prior (except for positive definiteness),
- Doubling the calibration uncertainty,
- Doubling the beam uncertainties.

The marginalized constraints resulting from these tests are listed in Table 6, and the posterior distributions are illustrated in Figure 20. The preference for negative running or more damping is robust to the systematic effects considered here. Doubling the calibration uncertainty has little impact on both parameters. Loosening the foreground priors slightly moves the $dn_s/d\ln k$ (Y_p) median to lower (higher) values with the uncertainty slightly broadened, which makes the preference a bit stronger. Doubling the beam uncertainties leads to stronger shifts and broadening of the constraints but the 2σ preference is almost unchanged.

In another test, we restrict the SPT bandpowers with $l_{\rm max} = 2200$ and $l_{\rm max} = 1500$. Combined with *WMAP*7 data, we obtain $dn_s/d\ln k = -0.025 \pm 0.013$ and $dn_s/d\ln k = -0.033 \pm 0.014$, respectively. The 2σ preference is robust within the range in which the extragalactic foregrounds are not important.

In summary, we find the preference in the data for less power at small scales to be robust to the multipole range and the foreground, beam and calibration priors.

Facilities: South Pole Telescope

REFERENCES

Aguilar, A., et al. 2001, Phys. Rev. D, 64, 112007
Aguilar-Arevalo, A. A., et al. 2010, Phys. Rev. Lett., 105, 181801
Anderson, L., et al. 2012, ArXiv e-prints, 1203.6594
Andersson, K., et al. 2011, ApJ, 738, 48
Aver, E., Olive, K. A., & Skillman, E. D. 2010, Journal of Cosmology and Astroparticle Physics, 5, 3
——. 2011, Journal of Cosmology and Astroparticle Physics, 3, 43
——. 2012, J. of Cosm. & Astropart. Phys., 4, 4
Bashinsky, S., & Seljak, U. 2004, Phys. Rev. D, 69, 083002
Bennett, C. L., et al. 2012, ArXiv e-prints, 1212.5225
Benson, B. A., et al. 2013, ApJ, 763, 147
Blake, C., et al. 2011, MNRAS, 418, 1707
Bond, J. R., Efstathiou, G., & Tegmark, M. 1997, MNRAS, 291, L33
Christensen, N., Meyer, R., Knox, L., & Luey, B. 2001, Classical and Quantum Gravity, 18, 2677
Chung, D. J. H., Shiu, G., & Trodden, M. 2003, Phys. Rev. D, 68, 063501
Cline, J. M., & Hoi, L. 2006, J. of Cosm. & Astropart. Phys., 6, 7
Conley, A., et al. 2011, ApJS, 192, 1

de Putter, R., et al. 2012, ApJ, 761, 12
Dicus, D. A., Kolb, E. W., Gleeson, A. M., Sudarshan, E. C. G., Teplitz, V. L., & Turner, M. S. 1982, Phys. Rev. D, 26, 2694
Doran, M., & Robbers, G. 2006, JCAP, 6, 26
Dunkley, J., et al. 2011, ApJ, 739, 52
Easther, R., & Peiris, H. V. 2006, J. of Cosm. & Astropart. Phys., 9, 10
Eisenstein, D. J., & Hu, W. 1998, ApJ, 496, 605
Fang, W., Hu, W., & Lewis, A. 2008, Phys. Rev. D, 78, 087303
Fendt, W. A., & Wandelt, B. D. 2007a, ArXiv:0712.0194
——. 2007b, ApJ, 654, 2
Feng, B., Li, M., Zhang, R.-J., & Zhang, X. 2003, Phys. Rev. D, 68, 103511
Finelli, F., Hamann, J., Leach, S. M., & Lesgourgues, J. 2010, J. of Cosm. & Astropart. Phys., 4, 11
Fixsen, D. J., Cheng, E. S., Gales, J. M., Mather, J. C., Shafer, R. A., & Wright, E. L. 1996, ApJ, 473, 576
Freedman, W. L., Madore, B. F., Scowcroft, V., Burns, C., Monson, A., Persson, S. E., Seibert, M., & Rigby, J. 2012, ApJ, 758, 24
Gando, et al., A. 2012, ArXiv e-prints, 1205.6130
Giunti, C., & Laveder, M. 2011, Physics Letters B, 706, 200
Goffe, W. L., Ferrier, G. D., & Rogers, J. 1994, Journal of Econometrics, 60, 65
Hamann, J., Hannestad, S., Lesgourgues, J., Rampf, C., & Wong, Y. Y. Y. 2010a, J. of Cosm. & Astropart. Phys., 7, 22
Hamann, J., Hannestad, S., Raffelt, G. G., Tamborra, I., & Wong, Y. Y. Y. 2010b, Phys. Rev. Lett., 105, 181301
Hamish Robertson, R. G. 2009, Journal of Physics Conference Series, 173, 012016
Hinshaw, G., et al. 2012, ArXiv e-prints, 1212.5226
Hou, Z., Keisler, R., Knox, L., Millea, M., & Reichardt, C. 2013, Phys. Rev. D, 87, 083008
Hu, W. 1998, Astrophys. J., 506, 485
Hu, W., & Dodelson, S. 2002, ARA&A, 40, 171
Ichikawa, K., Fukugita, M., & Kawasaki, M. 2005, Phys. Rev. D, 71, 043001
Ichiki, K., & Takada, M. 2012, Phys. Rev. D, 85, 063521
Izotov, Y. I., & Thuan, T. X. 2010, ApJ, 710, L67
Izotov, Y. I., Thuan, T. X., & Stasińska, G. 2007, ApJ, 662, 15
Kaiser, N. 1983, MNRAS, 202, 1169
Keisler, R., et al. 2011, ApJ, 743, 28
Kobayashi, T., & Takahashi, F. 2011, J. of Cosm. & Astropart. Phys., 1, 26
Komatsu, E., et al. 2011, ApJS, 192, 18
Kopp, J., Maltoni, M., & Schwetz, T. 2011, Physical Review Letters, 107, 091801
Kosowsky, A., & Turner, M. S. 1995, Phys. Rev. D, 52, 1739
Larson, D., et al. 2011, ApJS, 192, 16
Lewis, A., & Bridle, S. 2002, Phys. Rev. D, 66, 103511
Lewis, A., Challinor, A., & Lasenby, A. 2000, ApJ, 538, 473
Liddle, A. R., & Leach, S. M. 2003, Phys. Rev. D, 68, 103503
Lopez, R. E., Dodelson, S., Heckler, A., & Turner, M. S. 1999, Physical Review Letters, 82, 3952
Mangano, G., Miele, G., Pastor, S., Pinto, T., Pisanti, O., & Serpico, P. D. 2005, Nuclear Physics B, 729, 221
Mantz, A., Allen, S. W., & Rapetti, D. 2010, MNRAS, 406, 1805
Marshall, P., Rajguru, N., & Slosar, A. 2006, Phys. Rev. D, 73, 067302
Marulli, F., Carbone, C., Viel, M., Moscardini, L., & Cimatti, A. 2011, MNRAS, 418, 346
Mehta, K. T., Cuesta, A. J., Xu, X., Eisenstein, D. J., & Padmanabhan, N. 2012, ArXiv e-prints, 1202.0092
Mention, G., Fechner, M., Lasserre, T., Mueller, T. A., Lhuillier, D., Cribier, M., & Letourneau, A. 2011, Phys. Rev. D, 83, 073006
Moresco, M., Verde, L., Pozzetti, L., Jimenez, R., & Cimatti, A. 2012, J. of Cosm. & Astropart. Phys., 7, 53
Padmanabhan, N., Xu, X., Eisenstein, D. J., Scalzo, R., Cuesta, A. J., Mehta, K. T., & Kazin, E. 2012, ArXiv e-prints, 1202.0090
Peimbert, M., Luridiana, V., & Peimbert, A. 2007, ApJ, 666, 636
Pisanti, O., Cirillo, A., Esposito, S., Iocco, F., Mangano, G., Miele, G., & Serpico, P. D. 2008, Computer Physics Communications, 178, 956
Ratra, B., & Peebles, P. J. E. 1988, Phys. Rev. D, 37, 3406
Reichardt, C. L., de Putter, R., Zahn, O., & Hou, Z. 2012, ApJ, 749, L9
Reichardt, C. L., et al. 2013, ApJ, 763, 127
Reid, B. A., Verde, L., Jimenez, R., & Mena, O. 2010, Journal of Cosmology and Astroparticle Physics, 1, 3
Riemer-Sørensen, S., et al. 2012, Phys. Rev. D, 85, 081101
Riemer-Sørensen, S., Parkinson, D., Davis, T. M., & Blake, C. 2013, ApJ, 763, 89
Riess, A. G., et al. 2011, ApJ, 730, 119
Schramm, D. N., & Turner, M. S. 1998, Reviews of Modern Physics, 70, 303
Serenelli, A. M., & Basu, S. 2010, ApJ, 719, 865
Shaw, L. D., Nagai, D., Bhattacharya, S., & Lau, E. T. 2010, ApJ, 725, 1452
Shirokoff, E., et al. 2011, ApJ, 736, 61
Silk, J. 1968, ApJ, 151, 459
Simha, V., & Steigman, G. 2008, JCAP, 6, 16
Song, J., et al. 2012, ApJ, 761, 22
Steigman, G. 2007, Annual Review of Nuclear and Particle Science, 57, 463
Story, K. T., et al. 2013, ApJ, 779, 86
Sullivan, M., et al. 2010, MNRAS, 406, 782
Thomas, S. A., Abdalla, F. B., & Lahav, O. 2010, Physical Review Letters, 105, 031301
Tinker, J., Kravtsov, A. V., Klypin, A., Abazajian, K., Warren, M., Yepes, G., Gottlöber, S., & Holz, D. E. 2008, ApJ, 688, 709
Vikhlinin, A., et al. 2009, ApJ, 692, 1060
Wetterich, C. 1988, Nuclear Physics B, 302, 668
Zaldarriaga, M. ., & Harari, D. D. 1995, Phys. Rev. D, 52, 3276
Zaldarriaga, M., Spergel, D. N., & Seljak, U. 1997, ApJ, 488, 1+
Zhao, G.-B., et al. 2012, ArXiv e-prints, 1211.3741